

Effect of different good solvents in flash nano-precipitation via multi-scale population balance modeling-CFD coupling approach

*Original*

Effect of different good solvents in flash nano-precipitation via multi-scale population balance modeling-CFD coupling approach / Lavino, Alessio D.; Ferrari, Marco; Barresi, Antonello A.; Marchisio, Daniele. - In: CHEMICAL ENGINEERING SCIENCE. - ISSN 0009-2509. - STAMPA. - 245:(2021), p. 116833. [10.1016/j.ces.2021.116833]

*Availability:*

This version is available at: 11583/2910552 since: 2021-07-12T09:47:52Z

*Publisher:*

Elsevier

*Published*

DOI:10.1016/j.ces.2021.116833

*Terms of use:*

This article is made available under terms and conditions as specified in the corresponding bibliographic description in the repository

*Publisher copyright*

Elsevier postprint/Author's Accepted Manuscript

© 2021. This manuscript version is made available under the CC-BY-NC-ND 4.0 license  
<http://creativecommons.org/licenses/by-nc-nd/4.0/>. The final authenticated version is available online at:  
<http://dx.doi.org/10.1016/j.ces.2021.116833>

(Article begins on next page)

# Effect of Different Good Solvents in Flash Nano-Precipitation via Multi-scale Population Balance Modeling-CFD coupling approach

Alessio D. Lavino<sup>1</sup>, Marco Ferrari\*, Antonello A. Barresi, Daniele Marchisio

*Department of Applied Science and Technology, Institute of Chemical Engineering,  
Politecnico di Torino, 10129 Torino, Italy*

---

## Abstract

A computational and modeling approach is used to highlight the key factors that affect polymer nanoparticles (NP) formation in flash nano-precipitation (FNP), when the good solvent, e.g., acetone, is replaced by acetonitrile, tetrahydrofuran and tert-butanol. A population balance model is coupled with computational fluid dynamics to study the kinetics effects on FNP. The mean NP size is predicted in terms of mean radius of gyration via the Flory law of real polymers. The effect of different good solvents is modeled in terms of solute-solvent interactions, using the Flory-Huggins theory and Hansen solubility parameters. Promising results show how the proposed methodology is

---

*Abbreviations:* ACT, acetone; ACN, acetonitrile; CMD, cluster mass distribution; CFD, computational fluid dynamics; CIJM, confined impinging jets mixer; DQMOM-IEM, direct quadrature method of moments coupled with the interaction and exchange with the mean; FNP, flash nano-precipitation; HSP, Hansen solubility parameters; NP, Nanoparticles; PCL, poly- $\epsilon$ -caprolactone; PBM, population balance model; PDF, probability density function; QMOM, quadrature method of moments; TBA, tert-butanol; THF, tetrahydrofuran.

\*Corresponding author

*Email address:* `marco.ferrari@polito.it` (Marco Ferrari)

<sup>1</sup>Present address: Department of Chemical Engineering, Imperial College London, South Kensington Campus, London SW7 2AZ, UK

able to investigate the role played by different good solvents, analyzing single factors at the time. A deep insight into both the dynamics of mixing and the dynamics of aggregation is therefore reached and the main mechanisms involved are pointed out, showing a good agreement with experimental data.

*Keywords:* Flash Nano-Precipitation, Hansen Solubility Parameters, Flory-Huggins Theory, Population Balance Model, CFD

---

## 1. Introduction

Nanoparticles (NP) production has been widely investigated in the last decade, due to the wide range of its applications such as cosmetics, pharmaceuticals, textiles, agriculture, and food science (Das et al., 2009; Demetzos, 2016; Nelson, 2002; Prasad et al., 2014; Wu and Guy, 2009). The control of the final NP size and particle size distribution is of paramount importance, especially in controlled drug delivery systems applications, in which a threshold dimension must not be exceeded to guarantee the correct drug release at the targeted area inside the blood stream (Hans and Lowman, 2002; Petitti et al., 2008). In particular, polymer NP formation received a lot of attention from both experimental and modeling approaches, in order to determine the key parameters that govern the final NP targeted size (Celasco et al., 2014; Valente et al., 2012a,b; Zelenková et al., 2018). Due to their biological applications, polymers must be biocompatible and non-toxic; here, poly- $\epsilon$ -caprolactone (PCL) is used, since it has been considered one of the best candidates for this purpose (Who et al., 2000). One of the most used techniques for NP production is represented by the so-called flash nano-precipitation (FNP). It consists in the mixing of a ‘good solvent’ in which the

19 polymer is dissolved and a ‘bad solvent’ (also named as anti- or non-solvent),  
20 which is miscible with the good solvent but not compatible with the polymer.  
21 The anti-solvent destabilizes the mixture inducing polymer aggregation and  
22 precipitation of the formed NP. The phenomenon that governs NP forma-  
23 tion just described above is also labelled as solvent displacement (Saad and  
24 Prud’homme, 2016).

25 Several studies have been already carried out to understand fluid dynam-  
26 ics effects at macro- and micro-scales (Johnson and Prud’homme, 2003b;  
27 Liu and Fox, 2006) for the confined impinging jets mixer (Johnson and  
28 Prud’homme, 2003a) (CIJM) and also for different geometries, such as the  
29 vortex mixer (VM) (Marchisio et al., 2009, 2008), the multi-inlet vortex mixer  
30 (MIVM) (Liu et al., 2008), the T-mixer (Gradl et al., 2006) and the Y-mixer  
31 (Choi et al., 2005). Other experimental (Lince et al., 2008) and modeling  
32 (Cheng et al., 2010; Di Pasquale et al., 2012; Lavino et al., 2015, 2017) at-  
33 tempts also showed the importance of accounting for the kinetics besides  
34 the thermodynamics for FNP. However, numerous are still the open topics  
35 under debate that need to be addressed. One of them is represented by the  
36 effect of different good solvents in NP formation via FNP and has become  
37 a crucial aspect of the industrial NP production. Here, the interesting case  
38 of NP formation in CIJM is considered, with PCL as solute and water as  
39 anti-solvent. Four different good solvents are investigated: acetone (ACT),  
40 acetonitrile (ACN), tetrahydrofuran (THF) and tert-butanol (TBA).

41 The experimental procedure for polymeric NP production through solvent  
42 displacement has been extensively applied throughout the years, testing dif-  
43 ferent polymers; in particular, it was validated for PCL, obtaining also good

incorporation efficiency with different loading substances (Barresi et al., 2015; Celasco et al., 2014; Ferri et al., 2017; Lavino et al., 2019; Lince et al., 2008, 2009, 2011; Massella et al., 2018; Valente et al., 2012a,b; Zelenková et al., 2015, 2014). In experiments, water quenching (i.e. sudden dilution with distilled water) is employed as stabilization technique over time of the precipitated NP (Barresi et al., 2015; Ferri et al., 2017; Zelenková et al., 2015, 2014), preventing further aggregation in the reactor outlet (Barresi et al., 2015; Saad, 2007) and preserving the particle distribution. This is implicitly taken into account in our modeling approach by ‘freezing’ the predicted NP sizes at the outlet of the mixer (Lavino et al., 2017, 2019; Lince et al., 2009) allowing a consistent comparison with the experimental data, as it will be explained more clearly in the theoretical and modeling section of this work.

Experiments showed how different NP size and size distribution may be reached by just changing the good solvent (Ferri et al., 2017; Zelenková et al., 2015), a crucial aspect in several industrial contexts. At this level of description, from the experiments side, it is hard to fully understand the parameters that play a key role in determining different mean NP size at the outlet of the process. Hence, modeling and simulations are here employed to further examine those aspects and, eventually, to analyze them separately. A population balance model (PBM) which uses molecules as building blocks coupled with computational fluid dynamics (CFD) approach is used, already proposed and validated in an our previous work (Lavino et al., 2017), where the presence of the drug is neglected, as also in this present work. The main novelty of the proposed methodology consists in the incorporation of the thermodynamics theory of Flory-Huggins interaction parameter (Hansen, 2007) inside the ki-

netic model (PBM-CFD) to study the different good solvent effects on the  
 final predicted NP size. Recent efforts also showed at the molecular scale  
 the importance of accounting for the thermodynamics on the polymer con-  
 formation in mixtures (Gartner and Jayaraman, 2018; Lavino et al., 2018,  
 2020; Martin and Jayaraman, 2016). More specifically, the Flory-Huggins  
 interaction parameter  $\chi$  is here correlated to the mean radius of gyration,  
 expressed, in turn, in terms of Flory law (Flory, 1953). The solubility of PCL  
 is accounted for by using the Hansen solubility parameters (HSP) for the dif-  
 ferent solvents investigated in this work. This modeling approach brings the  
 advantage of considering thermodynamic quantities inside the kinetic model,  
 such as the Flory-Huggins  $\chi$  parameter and the HSP, extensively reported in  
 literature for a wide range of solvents and, more importantly, shows how to  
 correlate them to the prediction of the final mean NP size. In this way, it is  
 possible to readily obtain a transferable model, when different good solvents  
 are used in FNP. Kinetics and thermodynamics are therefore intertwined in  
 a unique modeling tool and used to investigate the effect of different good  
 solvents on NP precipitation, showing a promising way to reach a deeper  
 understanding of the Hansen approach, for the specific case of particulate  
 systems. Another very important advantage is the possibility to analyze sin-  
 gle factors at a time, unlike experiments, getting a deeper insight into the  
 main phenomena. In this way, the dynamics of mixing is studied separately  
 from the dynamics of aggregation, highlighting the physical and modeling  
 properties that mainly influence polymer aggregation, when different good  
 solvents are used.

The paper is structured as follows: modeling and theoretical backgrounds

are presented in section 2, with particular attention to the multi-scale kinetic model (CFD and population balance model) together with the thermodynamics of NP formation by solvent displacement; then, operating conditions and numerical details are reported in section 3. The main results are discussed in section 4 and, finally, conclusions and future developments are presented in section 5.

## 2. Theoretical Background

This section is dedicated to the theoretical background and the modeling strategy adopted in this work. The theory presented here is divided into two main subsections: *i.* the kinetic model, in which the main equations of the population balance model (PBM) and computational fluid dynamics (CFD) are presented; *ii.* the thermodynamic model, used to study the solute-solvent interactions, with a particular focus on the theory of real polymers in solution.

The PBM-CFD coupling approach is able to describe the effect of kinetics on NP precipitation by accounting for the interplay of many factors, such as the inlet flow rate, the turbulent mixing and the particles-collision dynamics (details thereof will be presented in section 2.1), which have been proven to strongly affect the final NP size at certain operating conditions (Lavino et al., 2017). More specifically, the PBM predicts the mean particles size at the outlet of the mixer, as well as the evolution of the particles size distribution, also named cluster mass distribution (CMD), as it will be labelled from now on. On the other hand, the thermodynamics of real polymers is used to build up a modeling bridge, able to embrace the different good solvent effects, and

118 strictly interconnected to the PBM, as it will be explained in section 2.2.

119     Regarding the flow field, the steady-state Favre-averaged continuity and  
120 Navier–Stokes equations are solved in the CFD code, together with the equa-  
121 tions for the turbulent kinetic energy,  $k$ , and the turbulent dissipation rate,  
122  $\varepsilon$ , in line with the standard  $k - \varepsilon$  turbulence model (Andersson et al., 2012).  
123 As these equations are very well known and already implemented in the CFD  
124 code, they are omitted here for a sake of brevity and the readers can refer to  
125 our previous work Di Pasquale et al. (2012) for further details. The Favre-  
126 average approach (Favre, 1965) is necessary, since two fluids with different  
127 densities are involved. The fluid can still be considered incompressible, but  
128 density fluctuations are taken into account in this way.

129     The effect of turbulent fluctuations on NP formation is modeled by the di-  
130 rect quadrature method of moments, coupled with the interaction-by-exchange-  
131 with-the-mean (DQMOM-IEM) method (Marchisio and Fox, 2005), in which  
132 two nodes/environments are employed for the quadrature procedure. Below,  
133 two subsections are dedicated respectively to the PBM (aggregation dynam-  
134 ics and micro-mixing models) and the thermodynamics of real polymers in  
135 solution, presenting the main modeling details employed in this work.

### 136 2.1. Population Balance Model for FNP

137     A population balance model (PBM) is employed to describe the evolution  
138 of the cluster mass distribution (CMD). Being this model extensively pre-  
139 sented in our previous work, here we report only the definition of the CMD  
140 and the kinetic equation in which the moments of the CMD are transported.  
141 For a complete detailed description of the PBM, please refer to Lavino et al.  
142 (2017). The CMD is modeled with a number density function,  $f(\mathbf{x}, n)$ , de-

143 fined in such a way that the quantity  $f(\mathbf{x}, n)dn$  represents the number den-  
 144 sity of NP, or molecular clusters, containing  $n$  macromolecules at position  $\mathbf{x}$ .  
 145 The term ‘macromolecule’ is here referred to as PCL molecule of molecular  
 146 weight  $M_W = 14000 \text{ g mol}^{-1}$ . The variable  $n$  is labelled as dimensionless  
 147 cluster mass or aggregation number and it can be treated as a continuous  
 148 variable, since it varies from one to very large numbers. In the pure good sol-  
 149 vent stream the PCL is completely dissolved and no aggregation takes place.  
 150 Therefore, the CMD corresponds to a Dirac delta function centred in  $n = 1$ .  
 151 By normalising the CMD with the Avogadro number (necessary to keep the  
 152 simulations numerically stable), the CMD in the good solvent stream (initial  
 153 conditions) corresponds to the initial polymer molar concentration.

154 The PBM is here solved with the quadrature method of moments (QMOM)  
 155 approach (Marchisio and Fox, 2013). Let us recall the definition of the generic  
 156  $j^{th}$ -order moment:

$$m^{(j)} = \int_0^\infty f(n)n^j dn. \quad (1)$$

157 The advantage is twofold: on one hand, the computational cost is heavily  
 158 reduced, compared to other discretized methods (Marchisio and Fox, 2013);  
 159 on the other hand, the moments of the CMD represent physical measur-  
 160 able quantities. Indeed,  $m^{(0)}$  is the total cluster number density,  $m^{(1)}$  is a  
 161 conserved quantity and corresponds to the total number density of macro-  
 162 molecules, whereas the ratio between  $m^{(1)}$  and  $m^{(0)}$  results in the average  
 163 number of macromolecules per NP or molecular cluster. Here the first four  
 164 moments are used (i.e.,  $j = 0, \dots, 3$ ), corresponding to a quadrature approx-  
 165 imation with two nodes.

166 By applying the moment transform and the Favre average  $\langle \cdot \rangle$ , the steady-  
 167 state transport equation for the  $j^{th}$ -order moment of the CMD  $f(n)$  reads as  
 168 follows:

$$\begin{aligned} \frac{\partial}{\partial \mathbf{x}} \cdot (\bar{\rho} \langle \mathbf{U} \rangle \langle m^{(j)} \rangle) - \frac{\partial}{\partial \mathbf{x}} \cdot \left( \bar{\rho} \Gamma_t \frac{\partial \langle m^{(j)} \rangle}{\partial \mathbf{x}} \right) = \\ = \frac{\bar{\rho}}{2} \left\langle \int_0^\infty \int_0^\infty \left[ (n + n')^j - n^j - n'^j \right] \beta(n, n') f(n) f(n') dn dn' \right\rangle, \quad (2) \end{aligned}$$

169 where  $\Gamma_t \approx \nu_t/0.7$ , is the turbulent diffusivity which is much larger than the  
 170 Brownian diffusivity and is calculated from the turbulent viscosity,  $\nu_t$ , by  
 171 assuming a turbulent Schmidt number of 0.7 (Andersson et al., 2012),  $\bar{\rho}$  is  
 172 the time-averaged fluid density and  $\langle \mathbf{U} \rangle$  is the Favre-averaged fluid velocity,  
 173 as the particle Stokes number is much less than unity (Baldyga and Orciuch,  
 174 2001). The aggregation kernel,  $\beta(n, n')$ , that appears in the source term on  
 175 the right hand side of Eq. (2) represents the rate with which two clusters  
 176 (or, equally, nanoparticles) collide and aggregate (second order point process  
 177 (Marchisio and Fox, 2013)). The source term consists of two contributions:  
 178 a negative term that states the disappearance of two clusters containing  
 179 respectively  $n$  and  $n'$  polymer macromolecules, and the appearance of the  
 180 aggregate cluster (positive term) formed by  $n + n'$  macromolecules. In line  
 181 with this purely-aggregative modelling approach, nucleation and growth do  
 182 not explicitly appear in the PBM formulation, which can be eventually taken  
 183 into account into the aggregation kernel (aggregation efficiency). This is a  
 184 direct consequence of the choice of the PBM internal variable which is  $n$ ,  
 185 number of molecules that belong to a cluster. For further details, please re-

186 fer to Lavino et al. (2017). It is noteworthy to stress that molecular dynamics  
 187 investigations (Di Pasquale et al., 2014) have shown that the freely-jointed  
 188 chain model (Rubinstein and Colby, 2003) can be applied in this mathemat-  
 189 ical formulation, so that a cluster made by  $n$  molecules of molecular weight  
 190  $M_w$  will behave as a cluster made by one single PCL molecule of molecular  
 191 weight  $n \cdot M_w$ . This assumption affects the formula used for the mean clusters  
 192 size, in terms of Flory law, as it will be shown in section 2.2.

193 The aggregation kernel accounts for two mechanisms: Brownian motions  
 194 and turbulent fluctuations. Here, the assumption is that these two contri-  
 195 butions are simply additive, and it holds on the physical evidence that at  
 196 low initial polymer concentration in good solvent stream, Brownian aggrega-  
 197 tion dominates over the turbulent one, and vice versa at high initial polymer  
 198 concentration. Applying the Stokes-Einstein formulation (Elimelech et al.,  
 199 1998), the aggregation kernel in function of the mean radius of gyration of  
 200 the two NP, or molecular clusters, that are self-assembling or aggregating  
 201 assumes the following expression (Cheng et al., 2010):

$$\begin{aligned} \beta(n, n') = \eta \frac{2k_B T}{3\mu} \frac{(\llbracket R_g(n, x_s) \rrbracket + \llbracket R_g(n', x_s) \rrbracket)^2}{\llbracket R_g(n, x_s) \rrbracket \llbracket R_g(n', x_s) \rrbracket} + \\ + 1.2944\eta \sqrt{\frac{\varepsilon}{\nu}} (\llbracket R_g(n, x_s) \rrbracket + \llbracket R_g(n', x_s) \rrbracket)^3, \quad (3) \end{aligned}$$

202 where  $\mu$  is the molecular viscosity of the suspending liquid (i.e. mixture  
 203 of the good and bad solvents and therefore function of the good solvent  
 204 molar fraction  $x_s$  (Lavino et al., 2017)),  $k_B$  is the Boltzmann constant,  $\varepsilon$  is  
 205 the turbulent dissipation rate,  $\nu$  is the mixture kinematic viscosity and  $\llbracket \cdot \rrbracket$

206 represents the ensemble-average.

207 The term  $\eta$  stands for an aggregation efficiency, only dependent on the  
208 initial supersaturation ratio. It is represented by a stepwise function: zero for  
209 undersaturated solutions and one for supersaturated solutions. The super-  
210 saturation ratio is defined as the ratio between the local PCL concentration  
211 and its equilibrium one. Their expressions are reported in our previous work  
212 (Lavino et al., 2017). When the supersaturation ratio is locally greater than  
213 unity, or in other words when the local PCL concentration is greater than its  
214 local solubility (i.e., equilibrium concentration), which in turn depends on  
215 the local solvent composition, self-assembly and aggregation are triggered;  
216 namely PCL molecular self-assemble forming NP that then further aggre-  
217 gate forming the final NP. The main assumption is that molecules are more  
218 stable when in a molecular cluster and therefore they self-assemble or aggre-  
219 gate irreversibly. This implies that the energy barrier for particle formation  
220 is null and therefore particle formation, under these conditions, can be in-  
221 terpreted as spinodal decomposition rather than nucleation. In line with the  
222 classical nucleation theory this model is applicable only when the initial su-  
223 persaturation is very large, as also found out in our previous work, where the  
224 model was originally validated by Lavino et al. (2017). An accurate quantifi-  
225 cation of the precipitated PCL with respect to what is left in solution during  
226 FNP still remains an unsolved issue; when the supersaturation ratio is much  
227 larger than unity, it is reasonable to assume that most of PCL precipitates  
228 out with the operating conditions investigated in this work.

229  $\llbracket R_g(n, x_s) \rrbracket$  represents the ensemble-averaged radius of gyration, depen-  
230 dent on the aggregation number  $n$  and on the good solvent molar fraction

231  $x_g$ . It is expressed in terms of the Flory law, as explained in subsection 2.2.  
 232 Moreover, the dynamics of mixing is also considered, as turbulence fluc-  
 233 tuations and local mixing gradients (supersaturation) affect PCL aggrega-  
 234 tion. More specifically, the solvent mixture fraction is described in terms of  
 235 probability density function (PDF) for the good solvent mass fraction,  $\xi$ , in  
 236 the good solvent-water mixture. As anticipated above in the text, mixing is  
 237 treated with the DQMOM-IEM approach with only two nodes/environments.  
 238 This turns out to be a strategic approach in modeling a binary mixture when  
 239 no reaction occurs (Di Pasquale et al., 2012; Gavi et al., 2007). In line with  
 240 the DQMOM-IEM, the weights and weighted abscissas in the two environ-  
 241 ments 1 and 2 are directly solved through suitable transport equations:

$$\frac{\partial}{\partial \mathbf{x}} (\bar{\rho} \langle \mathbf{U} \rangle p_1) - \frac{\partial}{\partial \mathbf{x}} \left( \bar{\rho} \Gamma_t \frac{\partial p_1}{\partial \mathbf{x}} \right) = 0, \quad (4)$$

242 and  $p_2 = 1 - p_1$  (the PDF integrates to unity), together with:

$$\begin{aligned} \frac{\partial}{\partial \mathbf{x}} (\bar{\rho} \langle \mathbf{U} \rangle p_1 \xi_1) - \frac{\partial}{\partial \mathbf{x}} \left( \bar{\rho} \Gamma_t \frac{\partial}{\partial \mathbf{x}} (p_1 \xi_1) \right) = \\ = \bar{\rho} \gamma_M p_1 p_2 (\xi_2 - \xi_1) + \frac{\bar{\rho} \Gamma_t}{\xi_1 - \xi_2} \left( p_1 \frac{\partial \xi_1}{\partial \mathbf{x}} \frac{\partial \xi_1}{\partial \mathbf{x}} + p_2 \frac{\partial \xi_2}{\partial \mathbf{x}} \frac{\partial \xi_2}{\partial \mathbf{x}} \right). \end{aligned} \quad (5)$$

243 The right-hand side of Equation (5) represents the molecular mixing, also  
 244 referred to as micro-mixing term, mathematically closed with the IEM ap-  
 245 proach (Fox, 2003);  $\gamma_M = \frac{C_\phi}{2} \frac{\varepsilon}{k}$  is the micro-mixing rate, where  $C_\phi$  is a pa-  
 246 rameter that depends on the local Reynolds number (Fox, 2003) and  $\varepsilon$  and  
 247  $k$  are respectively the turbulence dissipation rate and the turbulent kinetic

energy. More details can be found in Gavi et al. (2007). By inverting the subscripts 1 and 2, the transport equation related to  $p_2\xi_2$  can be obtained.  $\xi_1$  and  $\xi_2$  can be interpreted as local good solvent mass fractions in the two "environments", representing turbulent composition fluctuations. The Favre-averaged mass fraction can be calculated as follows:

$$\langle \xi \rangle = \int_0^1 p(\xi) \xi d\xi \approx p_1 \xi_1 + p_2 \xi_2, \quad (6)$$

where  $p(\xi)$  is the PDF related to the mixture fraction  $\xi$ . According to Equation (6), also the good solvent volume fraction can be defined as:

$$\langle \xi_v \rangle = p_1 \xi_{1,v} + p_2 \xi_{2,v}, \quad (7)$$

where  $\xi_{i,v}$  is the volume fraction in the environment  $i = 1, 2$ , function of the mass fraction through the relation  $\xi_{i,v} = [1 + (1/\xi_i - 1) \cdot \rho_s/\rho_w]^{-1}$ , with  $\rho_s$  and  $\rho_w$  the good solvent and water densities, respectively.

## 2.2. Thermodynamics of real polymers in solution

This section is referred to the thermodynamic model that is incorporated into the PBM-CFD model. Let us recall the Flory theory of real polymers in solution (Flory, 1953). The polymer conformation in a given mixture is the balance between attractive and repulsive forces among the repeated units, taken into account through the so called excluded volume  $v$ . The polymer conformation is strictly related to the nature of the solvent and, more specifically, the polymer mean squared radius of gyration, appearing in Eq. (3), can be expressed via the Flory law, that can in turn be extended to molecular clusters or NP containing  $n$  polymer molecules, as shown in our

268 previous work:

$$\llbracket R_g^2(n, x_s) \rrbracket = k_s(x_s)(nM_w)^{2\nu_s(x_s)}, \quad (8)$$

269 where, as mentioned, the freely-jointed chain hypothesis is applied for a  
 270 molecular cluster containing  $n$  PCL molecules,  $M_w$  is the molecular weight  
 271 of a single PCL molecule and  $k_s(x_s)$  and  $\nu_s(x_s)$  are the Flory parameters,  
 272 dependent, in turn, on the good solvent molar fraction  $x_s$  and on the na-  
 273 ture of the solvent, as indicated by the subscript  $s$ . As far as the acetone is  
 274 concerned as good solvent, molecular dynamics calculations have been per-  
 275 formed and interpolated and the corresponding functional forms determined  
 276 in a previous work (Di Pasquale et al., 2014):

$$k_s(x_s) = k_{ref}(x_{ref}) = 0.0064 \exp(-3.15x_{ref}), \quad (9)$$

$$\nu_s(x_s) = \nu_{ref}(x_{ref}) = 0.30 + 0.45x_{ref} - 0.15x_{ref}^2, \quad (10)$$

277 where the subscript '*ref*' is introduced and from now on it will refer to as the  
 278 reference solvent, namely the solvent for which all the necessary information  
 279 is already provided from previous studies (acetone in this case).

280 When the repulsive forces dominate on the attractive ones among the  
 281 monomers, the excluded volume  $v$  assumes a positive value and the polymer  
 282 shows a more stretched (coil) conformation, corresponding to a good solvent  
 283 condition, and the Flory exponent is equal to  $3/5$ . On the contrary, when  
 284 the monomer attractive forces prevail, the excluded volume  $v$  is negative and  
 285 the polymer exhibits a globule conformation. The latter case corresponds to

286 a bad solvent condition and the Flory exponent is equal to  $1/3$ . When the  
 287 two forces counterbalance each other, the excluded volume is null and the  
 288 polymer assumes an ideal conformation, related to the so called ' $\theta$ -condition'.  
 289 At the  $\theta$ -condition, the Flory exponent is equal to  $1/2$ . The close proximity to  
 290 the bad solvent condition is crucial to be locally reached in FNP, in order to  
 291 induce the spontaneous self-assembly of the polymer molecules in molecular  
 292 cluster or NP.

293 As a matter of fact, then, the polymer conformation is strictly depen-  
 294 dent on the nature of the surrounding solvent; therefore, the Flory-Huggins  
 295 interaction parameter,  $\chi_{s,p}$ , is introduced in this modeling framework, being  
 296 this one a direct measure of the energetic interaction of two components, e.g,  
 297 a solute  $p$  and a solvent  $s$ , in turn, strictly correlated to the solubility of  
 298 the solute in that specific solvent. The solubility is here taken into account  
 299 by using the Hansen solubility parameters (HSP). The model presented in  
 300 this work correlates the radius of gyration with the interaction parameter  $\chi$   
 301 and the HSP, in order to be able to properly define the Flory parameters  
 302 ( $k_s(x_s)$  and  $\nu_s(x_s)$ ) functional forms in Eq. (8), when different good solvents  
 303 are employed.

304 Before getting into the HSP theory, a brief mention to the Hildebrand  
 305 approach is mandatory. The Hildebrand solubility parameter (Hildebrand  
 306 and Scott, 1950) of a substance corresponds to the cohesive energy per unit  
 307 volume (it quantifies the work necessary to keep molecules close to each  
 308 other) and reads as follows:

$$\delta = \left( \frac{\Delta H_v - RT}{V} \right)^{1/2}, \quad (11)$$

309 where  $\Delta H_v$  is the vaporization enthalpy,  $R$  is the gas constant,  $T$  is the  
310 absolute temperature and  $V$  is the molar volume.

311 Hansen (2007) proposed a decomposition of the Hildebrand parameter  
312 into three different contributions, leading to the so-called Hansen solubility  
313 parameters (HSP):

$$\delta = (\delta_D^2 + \delta_P^2 + \delta_H^2)^{1/2}, \quad (12)$$

314 where  $\delta_D$  considers the dispersion attractive forces (non-polar),  $\delta_P$  accounts  
315 for the permanent dipole-permanent dipole interactions and  $\delta_H$  for the hy-  
316 drogen bonds. The main advantage of the HSP approach is that polar effects  
317 are explicitly considered, differently from the Hildebrand parameter that is  
318 more suitable for apolar systems. The ability of a given solvent to solubilize  
319 a solute (e.g., polymer) is expressed in terms of solubility ‘distance’ from the  
320 solute itself and takes the form of the radius of a sphere in Hansen solubility  
321 space  $\{\delta_D, \delta_P, \delta_H\}$  (Hansen, 2007):

$$Ra^2(\delta) = 4(\delta_{D,s} - \delta_{D,p})^2 + (\delta_{P,s} - \delta_{P,p})^2 + (\delta_{H,s} - \delta_{H,p})^2, \quad (13)$$

322 where  $Ra(\delta)$  is the solubility ‘distance’, in terms of sphere radius in the  
323 Hansen space, and the subscripts  $s$  and  $p$  refer respectively to the solvent  
324 and the polymer. The term ‘4’ is added in order to make the shape of this  
325 functional form more spherical and less elliptical. The whole derivation can  
326 be found in Hansen (2007). The Flory-Huggins parameter relative to the  
327 interaction between the solvent and the polymer  $\chi_{s,p}$  can be expressed as a

328 function of the HSP through:

$$\chi_{s,p} = \frac{1}{2} \cdot \left( \frac{Ra(\delta)}{2R_m} \right)^2, \quad (14)$$

329 where  $Ra(\delta)$  is the solubility distance, function of the HSP, as reported in  
 330 Eq. (13) and  $R_m$  represents the radius of the solubility sphere, namely the  
 331 maximum solubility distance (in Hansen solubility space) that allows the sol-  
 332 vent to dissolve the solute. It is worthwhile to stress again that in Hansen  
 333 phase space the coordinates are square roots of energies per unit volume;  
 334 therefore, talking about ‘solubility distances’ refers implicitly to ‘energetic  
 335 distances’ contributions between two components. The parameter  $R_m$  is de-  
 336 fined in such a way that the dependence of the solubility parameters on the  
 337 polymer molecular weight is accounted for, thanks to the following expres-  
 338 sion:

$$R_m^2 = 0.5(1 + 1/r^{1/2})RT/V_m, \quad (15)$$

339 where  $V_m$  is the molar volume of the solvent and  $r$  is the degree of poly-  
 340 merization, which can be calculated as the ratio between the total PCL  
 341 macromolecule and the single repeated unit molecular weights.

342 Solvents characterized by  $Ra > 2R_m$  are classified as non-solvents (or bad  
 343 solvents) with respect to that specific solute. On the contrary, all the solvents  
 344 that belong to the Hansen solubility sphere ( $Ra/2R_m$  smaller than unity)  
 345 are classified as good solvents for that solute. In terms of  $\chi_{s,p}$  interacting  
 346 parameter, what stated above is equivalent to infer that when  $\chi_{s,p} < 1/2$  the  
 347 system is in good solvent condition, namely the solute molecule shows a more

348 stretched conformation because the solvent-solute interactions are preferred  
 349 over the solute-solute ones;  $\chi_{s,p} > 1/2$  corresponds to bad solvent condition,  
 350 namely the solute molecule shows a more globule conformation because the  
 351 solute-solute interactions are preferred over the solvent-solute ones;  $\chi_{sp} =$   
 352  $1/2$  is the  $\theta$ -condition, corresponding to ideal conformation of the solute  
 353 molecule occurring when the solute-solvent and solute-solute interactions are  
 354 energetically equivalent.

355 As stated above, it is the local close proximity to bad solvent condition  
 356 that energetically (and also entropically) drives the spontaneous PCL self-  
 357 assembly. Under these conditions, the radius of gyration of a single polymer  
 358 molecule,  $R_g$ , can be expressed as a function of the Flory-Huggins parameter,  
 359  $\chi_{s,p}$  (Rubinstein and Colby, 2003):

$$R_g \approx \frac{b^2}{|v|^{1/3}} N^{1/3} = \frac{bN^{1/3}}{(2\chi_{s,p} - 1)^{1/3}}, \quad (16)$$

360 where  $b$  is the Kuhn length (representative of the monomer length) and  $N$   
 361 is the number of repeated units that form the polymer chain. The expres-  
 362 sion reported in Eq. (16) is for real polymers in solution, since the negative  
 363 excluded volume  $v$  is taken into account, as well as the Flory exponent  $1/3$   
 364 appears, meaning that the single polymer molecule is surrounded by a bad  
 365 solvent.

366 Starting from the relationship reported in Eq. (14), combined with Eq. (16),  
 367 the whole procedure to find the Flory parameters functional forms for an un-  
 368 known good solvent is developed and extensively explained in the following  
 369 section.

### 370 **3. Operating conditions and numerical details**

#### 371 *3.1. Experimental background*

372 Details about the experimental set-up which this modeling work is based  
373 on are here reported. As already stated, PCL is the polymer employed as so-  
374 lute in the FNP process investigated in this work. It is especially suitable for  
375 NP production in the pharmaceutical field and for biological applications,  
376 since PCL is bio-compatible and non-toxic (Who et al., 2000); among the  
377 other advantages, it is also permeable to low molecular weight drugs and can  
378 therefore be used for diffusion controlled delivery systems (Le Roy Boehm  
379 et al., 2000). The experimental procedure for PCL NP production has been  
380 extensively validated throughout the years (Barresi et al., 2015; Celasco et al.,  
381 2014; Ferri et al., 2017; Lavino et al., 2019; Lince et al., 2008, 2009, 2011;  
382 Massella et al., 2018; Valente et al., 2012a,b; Zelenková et al., 2015, 2014).  
383 In the experimental context, the NP stabilization over time is of paramount  
384 importance and, in order to prevent further aggregation at the mixer outlet  
385 (Barresi et al., 2015; Saad, 2007) and to preserve the particle size distribu-  
386 tion, the outlet CIJM stream is usually quickly diluted in ultra-pure water  
387 and gently stirred to stabilize the NP suspension. Dilution, also labelled as  
388 ‘quench’, avoids the size increase due to Ostwald ripening effects (Barresi  
389 et al., 2015; Ferri et al., 2017; Zelenková et al., 2015, 2014) and keeps the  
390 precipitated NP stable up to 20 days (Le Roy Boehm et al., 2000). The  
391 water quench volume can have an effect of the final NP size (Barresi et al.,  
392 2015; Ferri et al., 2017), therefore all the experimental data shown here are  
393 obtained by quenching with the same water amount.

394 Although several polymers have been tested for NP production via FNP

(Saad, 2007), very little experimental data are available in literature - to the best of the authors knowledge - showing the effect of different good solvents for the same specific type of polymer. As this represents the aim of this work, only experimental studies using PCL as polymer solute have produced enough data to guarantee a consistent comparison with our modeling results.

The experimental measurements were conducted via Dynamic Light Scattering (DLS) in diluted samples. By means of this technique the hydrodynamic radius,  $R_H$ , is estimated as the ratio between the 7<sup>th</sup>- and the 6<sup>th</sup>-order moments of the NP distribution. However, from our modeling point of view, those quantities can be determined only with a numerical regression since the highest order moment we solve numerically is of order three (only two nodes in the aggregation model solved via QMOM). Therefore, it turns out to be more reasonable to express the mean particle size in terms of ratio between 1<sup>st</sup>- and 0<sup>th</sup>-order moments of the radius of gyration,  $R_g$ , distribution. Despite the hydrodynamic radius is generally greater than the radius of gyration (Bhattacharjee, 2016), we made the approximation:  $R_H \approx R_g$  which holds particularly for spherical NP. Ultimately, it is an acceptable assumption for narrow CMD characterized by small poly-dispersity indexes (Barresi et al., 2015; Ferri et al., 2017).

### 3.2. Experimental set up

Four different good solvents are investigated in this work: acetone (ACT), acetonitrile (ACN), tetrahydrofuran (THF) and tert-butanol (TBA). As stated above, the acetone is labelled as the reference solvent, since a full modeling description thereof was already provided from previous molecular dynamics (Di Pasquale et al., 2014) and CFD simulations (Di Pasquale et al., 2012;

420 Lavino et al., 2017). The geometrical dimensions of CIJM are: inlet and out-  
 421 let diameters respectively equal to 1 and 2 mm. The width of the chamber  
 422 is equal to 4.76 mm and its height is two times the width, in line with our  
 423 previous work (Di Pasquale et al., 2012; Lavino et al., 2017).

### 424 3.3. Numerical details

425 Ansys Fluent 15 is used in this work and the QMOM and DQMOM-  
 426 IEM routines are implemented via suitable user-defined functions (UDF)  
 427 and scalars (UDS). The computational grid consists of about 120.000 uni-  
 428 form hexahedral cells (for half of the actual geometry); a grid refinement  
 429 is present near the impinging plane and in the region around the two in-  
 430 let flows. The SIMPLE algorithm is used for the pressure-velocity coupling,  
 431 whereas spatial discretization is treated with the first-order upwind scheme.  
 432 Turbulence inside the mixer is modelled via the standard  $k - \varepsilon$  with en-  
 433 hanced wall treatment near the wall, as this can be considered an adequate  
 434 approach for this system (Gavi et al., 2007). Outlet boundary conditions are  
 435 set to zero normal gradients for all flow variables, except for pressure; in this  
 436 way, outflow boundary values are not imposed but are calculated from the  
 437 interior. The geometrical details of the simulated domain correspond to the  
 438 ones reported in the previous subsection. The initial values of the moments  
 439 of the CMD,  $m^{(j)}$ , are linked to the initial PCL concentration through the  
 440 relationship:  $m^{(j)} = c_{in}^{PCL} \rho / (M_w \rho_s)$ , where  $c_{in}^{PCL}$  represents the initial PCL  
 441 concentration in good solvent stream (expressed in  $\text{mg mL}^{-1}$ ),  $M_w$  is the  
 442 PCL molecular weight,  $\rho_s$  and  $\rho$  are the good solvent and the mixture den-  
 443 sity (see Lavino et al. (2017)), respectively. The aforementioned relationship  
 444 turns out to be independent of the moments order  $j = 0, \dots, 3$ , as the PCL is

initially dissolved in the good solvent (stable conditions) and, consequently, the corresponding CMD is a Dirac delta centred in  $n = 1$ . According to the quadrature-based moments method employed in this work, the mean radius of gyration of a population of NP,  $\langle R_g \rangle$ , is calculated as follows:

$$\langle R_g \rangle = \frac{\sum_{\alpha=1}^N \llbracket R_g(n_\alpha) \rrbracket}{\sum_{\alpha=1}^N \omega_\alpha}, \quad (17)$$

where  $\omega_\alpha$  and  $n_\alpha$  are the weights and nodes of the quadrature approximation calculated from the moments of the CMD:  $m^{(j)}$ , where for  $N = 2$  we have:  $j = 0, \dots, 3$ . It is worth stressing that  $\langle R_g \rangle$  is the mean radius of gyration of a population of nanoparticles, each characterized by its own individual ensemble-averaged radius of gyration, indicated as  $\llbracket R_g^2(n) \rrbracket$  in Eq. (8). The comparison with experiments is done in terms of  $\langle R_g \rangle$  exiting the CIJM. As stated above, during experiments the aggregation is limited and the particles are stabilized by quench water immediately after precipitation, preventing in this way further aggregation. It is reasonable to conclude, therefore, that measuring an average property at the outlet of the mixer from our simulations is totally equivalent to measure experimentally the given property immediately after quenching, via dynamic light scattering. However, it is worthwhile to mention that uncertainties present in the current work and the derivation of the models (Flory parameters, aggregation kernel, etc.) keep the predicted NP dimensions always included into the uncertainty range of the experimental results (Ferri et al., 2017; Lavino et al., 2017).

It is important to stress here that the choice of the good solvent has multiple effects on the FNP process. Indeed, by changing the good solvent we simultaneously change the thermodynamics of the interaction between the

polymer chains and the good solvent and bad solvent mixture, the kinetics of polymer molecule self-assembly and the dynamics of mixing of the two feed streams (i.e., good and bad solvent). As mentioned in the introduction, the main objective of this work is to quantify each of these effects (on the final NP size and CMD) separately.

Density, viscosity and molar volume of the good solvents represent the physical-chemical properties that are expected to play a role in the FNP process. The density of the good solvent affects the fluid dynamics in the CIJM and the position of the impinging plane. The viscosity of the good solvent determines, via the Stokes-Einstein law already included in the aggregation kernel reported in Eq. (3), the kinetics of molecules and molecular cluster self-assembly/aggregation. The molar volume of the good solvent defines the final good solvent molar fraction (for a given volume ratio between good and bad solvents). They are schematically listed in Table 1.

Table 1: Physical-chemical properties of the good solvents, Reynolds number,  $Re_s$ , range and initial PCL concentrations investigated in this work. The good solvent-to-water inlet flow rate ratio is equal to unity.

Good solvent	Density, $\text{kg m}^{-3}$	Viscosity, $\text{Pa}\cdot\text{s}$	Molar volume, $\text{cm}^3\text{mol}^{-1}$	$Re_s$ range <sup>a</sup>	Initial PCL concentration, $\text{mg mL}^{-1}$		
ACT	780.85	$3.10 \times 10^{-4}$	74.38	1069 – 6414	3.0	6.0	9.0
ACN	771.45	$3.26 \times 10^{-4}$	53.21	1004 – 6026	3.0	6.0	9.0
THF	874.78	$4.34 \times 10^{-4}$	82.43	855 – 5133	3.0	5.0	
TBA	777.89	$3.46 \times 10^{-3}$	95.29	95 – 573		5.0	

<sup>a</sup>  $Re_s$  refers to the good solvent inlet jet stream (see Eq. (18)), ranging from 20 to 120  $\text{mL min}^{-1}$ .

As it can be seen in Table 1, acetone and acetonitrile have similar values of density and viscosity; instead, acetonitrile has a smaller molar volume; this may become a crucial factor that affects the mean NP size, as it will be shown in section 4. On the contrary, THF has higher density, viscosity

486 and molar volume with respect to acetone and acetonitrile. More generally,  
 487 despite all the solvents investigated here present similar physical properties,  
 488 it is noteworthy to stress that TBA exhibits one order of magnitude higher  
 489 viscosity. The way in which the density fluctuations are taken into account,  
 490 as well as the local viscosity and molar fraction dependence on molar volumes,  
 491 are reported in an our previous work (Lavino et al., 2017), and therefore here  
 492 omitted for the sake of brevity.

493 Although experiments and simulations are conducted by varying the inlet  
 494 flow rate, the mean radius of gyration of the NP exiting the CIJM is evaluated  
 495 as a function of Reynolds number,  $Re_s$ , referred to the good solvent inlet jet  
 496 stream and its definition reads as follows:

$$Re_s = \frac{\rho_s d_{in} u_j}{\mu_s} \quad (18)$$

497 where  $d_{in}$  is the CIJM inlet diameter,  $u_j$  is the mean inlet jet velocity,  $\rho_s$   
 498 and  $\mu_s$  are the good solvent density and viscosity respectively, as reported  
 499 in Table 1. When comparing the dynamics of aggregation for different good  
 500 solvents, the Reynolds number includes the inlet operating conditions as well  
 501 as the physical properties of the good solvent to make the outcome of this  
 502 work a general discussion, as it will be clearer in section 4.

503 Solvents and polymer Hansen solubility parameters (HSP), as well as the  
 504 corresponding distances from PCL,  $Ra$ , are listed in Table 2.

505 The distances from PCL are representative of the solvent affinity with  
 506 the polymer. More specifically, the lower is the distance (last column in  
 507 Table 2), the higher is the solvent-solute affinity. As expected, the water sol-  
 508 ubility distance is the highest value, much higher than the Hansen solubility

Table 2: Hansen solubility parameters (HSP) and distances,  $Ra$ , from PCL (Eq. (13)) for all the components of the investigated system.

	$\delta_D$ , MPa <sup>1/2</sup>	$\delta_P$ , MPa <sup>1/2</sup>	$\delta_H$ , MPa <sup>1/2</sup>	$Ra$ , MPa <sup>1/2</sup>
PCL	17.0	4.8	8.3	-
THF	16.8	5.7	8.0	1.0
ACT	15.5	10.4	7.0	6.5
TBA	15.2	5.1	14.7	7.4
ACN	15.3	18.0	6.1	13.8
Water	15.6	16.0	42.3	35.9

sphere radius for PCL,  $R_m \approx 9.8$  MPa<sup>1/2</sup> (calculated by means of swelling  
 tests Bordes et al. (2010)), proving therefore to behave as bad solvent. In  
 the Hansen phase space, acetone, THF and TBA belong to the Hansen sol-  
 ubility sphere, behaving as good solvents. In the case of acetonitrile, the  
 distance from PCL is shown to be slightly higher than the sphere radius.  
 It is worthwhile mentioning that Bordes et al. (2010) obtained this value of  
 $R_m$  by performing swelling tests in which PCL initial concentration was two  
 orders of magnitude higher than the one employed in this work. It is there-  
 fore reasonable to assume that  $R_m$  would be much higher in this context,  
 so that also acetonitrile leads to a full PCL solubilization, as seen in our  
 experiments (Ferri et al., 2017), and consequently behaving as good solvent  
 in these operating conditions.

In this analysis, the solute is the PCL and the solvent is the ‘good solvent-  
 water’ mixture. Being the second phase made by a binary mixture, all the  
 solubility parameters (e.g., HSP) and physical properties (e.g., molar volume)  
 involved in the following calculations are weighted on the good-bad solvents  
 volume and molar fractions. The binary mixture phase will be therefore

generically labelled as ‘solvent’ from now on. The single PCL macro-molecule molecular weight  $M_w = 14000 \text{ g mol}^{-1}$  and the repeated unit molecular weight  $M_o = 114 \text{ g mol}^{-1}$ . The term  $r$  appearing in Eq. (13) corresponds to the degree of polymerization, here simply evaluated as  $M_w/M_o$ .

Let us recall that in FNP the PCL solubility limit is overcome and the self-assembly induced only thanks to the presence of the bad solvent, which is a local effect. Furthermore, the mixing is generally very fast and efficient, leading to a well micro-mixed system in almost all the domain of the CIJM (Gavi et al., 2007). Hence, the assumption of considering the polymer chain at the mean good solvent molar fraction  $\bar{x}_s$  holds, after mixing occurs, in the range  $\bar{x}_s \in [0.15, 0.25]$  for all the good solvents, since the good solvent-to-water ratio in volume is constant and equal to unity. Consequently, the three-components phase diagram (water, good solvent and PCL) can be approximated as a two-components one (the polymer as solute and the binary mixture as solvent) (Flory, 1953). In these conditions, the single PCL radius of gyration dependence on  $\chi_{s,p}$  can be expressed by means of Eq. (16), since the binary mixture behaves as a bad solvent, leading the single macro-molecules to self-assemble. This concept will be confirmed by looking at the  $\chi_{s,p}$  values, reported in Table 3 later on.

By using the relation reported in Eq. (16) for two different solvents  $s1$  and  $s2$  (e.g.,  $s1 = \text{acetonitrile-water}$  and  $s2 = \text{acetone-water}$ ), and assuming that the Kuhn length  $b$  (mainly a solute property) does not change too much for any solvent used, the following ratio can be readily obtained:

$$\frac{\llbracket R_g(n=1) \rrbracket_{s1}}{\llbracket R_g(n=1) \rrbracket_{s2}} \approx \frac{(2\chi_{s2,p} - 1)^{1/3}}{(2\chi_{s1,p} - 1)^{1/3}} = S_f, \quad (19)$$

where  $S_f$  is a scaling ratio, function of the solely Flory-Huggins parameters  $\chi_{s1,p}$  and  $\chi_{s2,p}$ , calculated starting from the HSP through Eq. (14). The adopted strategy consists in setting  $s2$  as the reference solvent, i.e., acetone-water in this case, for which the functional forms of Flory parameters are known from MD (Di Pasquale et al., 2014). By rearranging Eq. (19) as a function of the reference solvent, the following equality holds:

$$\sqrt{k_{s1}(x_{s1})M_w^{2\nu_{s1}(x_{s1})}} = S_f \cdot \sqrt{k_{ref}(x_{ref})M_w^{2\nu_{ref}(x_{ref})}}, \quad (20)$$

where, as stated above, the subscript *ref* refers to the acetone-water mixture. Scaling factors  $S_f$  and Flory-Huggins parameters  $\chi_{s,p}$  referred to the solvent-polymer systems investigated in this work, namely acetone-water, acetonitrile-water, THF-water and TBA-water, evaluated at mean good solvent molar fraction  $\bar{x}_s$ , are reported in Table 3.

Table 3: Flory-Huggins parameter,  $\chi_{s,p}$ , for acetone, acetonitrile, THF and TBA as good solvents with the relative scaling factors obtained from Eq. (19), at mean good solvent molar fraction,  $\bar{x}_s$ .

Solvent	$\bar{x}_s$	Flory-Huggins parameter,	Scaling factor,
		$\chi_{s,p}$	$S_f$
ACT-water	0.20	0.926	1.00
ACN-water	0.25	1.007	0.94
THF-water	0.18	0.873	1.05
TBA-water	0.16	1.251	0.83

By looking at Table 3, the Flory-Huggins parameter is always greater than  $1/2$  ( $\theta$ -condition) for each solvent investigated here. This confirms what was already stated above: the systems are in bad solvent conditions and the single PCL macromolecules are spontaneously led to aggregate.

At this point, an iterative procedure can be carried out, based on Eq. (20) and on the values reported in Table 3. More specifically, Eq. (20) still presents two degrees of freedom, that are the Flory constant and exponent functional forms. By putting  $\nu_{s1}(x_{s1}) = \nu_{ref}(x_{s1})$  as starting value,  $k_{s1}(x_{s1})$  is univocally determined and with this new set of Flory parameters, say  $k_{s1}^*(x_{s1})$  and  $\nu_{s1}^*(x_{s1})$ , simulations can be performed and the deviation against the experimental data is detected. Based on the deviation with respect to experiments, the Flory exponent is suitably adjusted to a new functional form, say  $\nu_{s1}^{**}(x_{s1})$  and, by means of Eq. (20), a new functional form for  $k_{s1}^{**}(x_{s1})$  is obtained. With this new set of Flory parameters, simulations are performed until this iterative procedure leads to an acceptable accordance against experiments. This corresponds to the Flory parameters reported in Table 4.

Table 4: Flory parameters functional forms for acetone (reported in Eq. (9) and (10)), acetonitrile, THF and TBA.

Good solvent	$k_s(x_s)$	$\nu_s(x_s)$
<b>ACT</b>	$0.0064 \exp(-3.15x_s)$	$0.30 + 0.45x_s - 0.15x_s^2$
<b>ACN</b>	$0.0055 \exp(-3.15x_s)$	$0.30 + 0.40x_s - 0.10x_s^2$
<b>THF</b>	$0.0047 \exp(-3.15x_s)$	$0.30 + 0.62x_s - 0.32x_s^2$
<b>TBA</b>	$0.0056 \exp(-3.15x_s)$	$0.30 + 0.42x_s - 0.12x_s^2$

The adjustment of the Flory parameters functional forms deserves further explanations. Regarding the Flory constant,  $k_s(x_s)$ , only the proportionality constant of the exponential is adjusted with respect to the function referred to acetone, Eq. (9). As far as the Flory exponent  $\nu_s(x_s)$  is concerned, it corresponds to a parabolic profile (Eq. (10)); therefore, three conditions are needed: two of them are represented by the exponent value in pure good and pure bad solvent, that are respectively 3/5 and 1/3, in line with the

583 Flory theory. The third condition is the only degree of freedom that the  
 584 user needs to fulfill and it might correspond to its value at the mean good  
 585 solvent molar fraction,  $\nu_s(\bar{x}_s)$ , that is suitably adjusted during the iterative  
 586 procedure presented above.

## 587 4. Results

588 First, only the dynamics of mixing is shown in order to assess the im-  
 589 portance of changes in physical properties when different good solvents are  
 590 used in FNP. In Figure 1 two quantities related respectively to macro- and  
 591 micro-mixing are reported for all the four solvents investigated here and for  
 592 two feeding flow rates. The first one is represented by the good solvent vol-  
 593 ume fraction,  $\langle \xi_v \rangle$  (see Eq. (7)). It is clear how in general the macro-mixing  
 594 is very efficient for all the solvents since in almost the whole domain  $\langle \xi_v \rangle$   
 595 approaches to 0.5, as expected by using an inlet volume flow rate ratio equal  
 596 to unity. Two different flow rates are here considered: 40 mL/min and 100  
 597 mL/min. Further mathematical details about the macro-mixing are reported  
 598 in Appendix A.

599 Besides macro-mixing, it is worthwhile to evaluate also the micro-mixing,  
 600 being this one a fundamental aspect of FNP (Di Pasquale et al., 2012). As  
 601 already mentioned, the mixture fraction is modeled via the DQMOM-IEM  
 602 for which the corresponding transport equation is reported in section 2.1. A  
 603 particular focus is given now to the micro-mixing term of that transport equa-  
 604 tion which corresponds to  $\gamma_M p_1 p_2 (\xi_2 - \xi_1)$ , where  $\gamma_M$  is the micro-mixing  
 605 rate, namely expressing the rate with which good solvent and bad solvent  
 606 mix at the molecular level.  $p_i$  and  $\xi_i$  correspond respectively to the weights

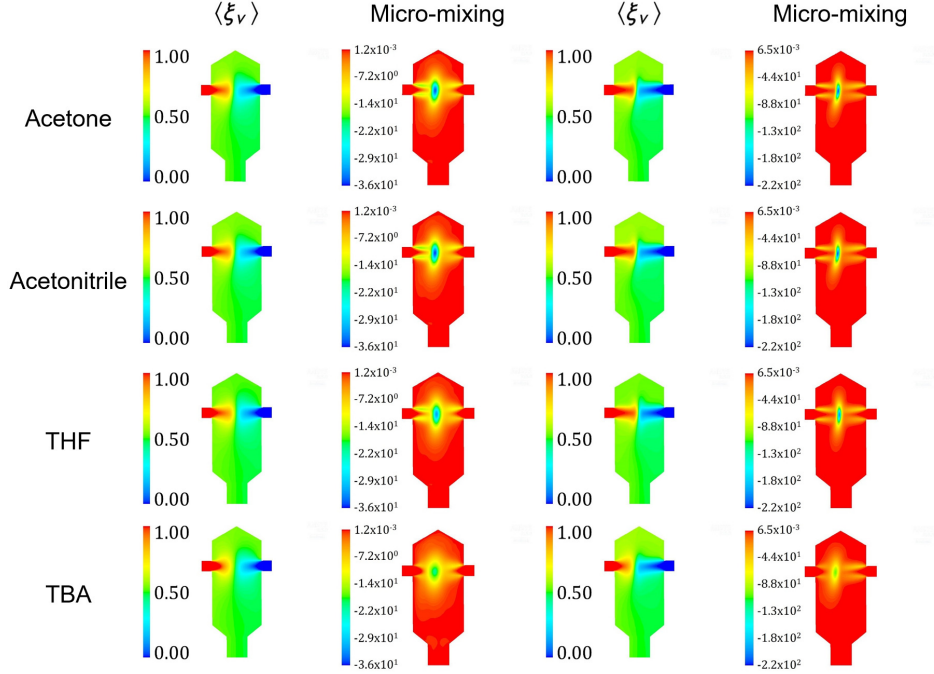


Figure 1: Good solvent volume fraction,  $\langle \xi_v \rangle$  (Eq. (7)), and micro-mixing term,  $\gamma_{MP1P2}(\xi_2 - \xi_1)$  (Eq. (A.4)), for which a further mathematical and physical analysis is reported in section 2.1 and in Appendix A. Two inlet flow rates are here reported: 40 mL min<sup>-1</sup> (left side) and 100 mL min<sup>-1</sup> (right side).

and abscissas (or nodes, or environments) of the quadrature formula, in the two environments  $i = 1, 2$ , in line with the DQMOM approach (Marchisio and Fox, 2005). The whole micro-mixing term describes how fast the micro-mixing variance is dissipated by turbulence (Fox, 2003; Liu and Fox, 2006). The entire mathematical framework is here omitted, being already presented in our previous works (Di Pasquale et al., 2012; Lavino et al., 2017) and a further mathematical elaboration is provided in Appendix A, in which the

614 relationship between micro-mixing term and micro-mixing variance is clearly  
615 stated.

616 At this level of description, Figure 1 points out that the micro-mixing term  
617 is very similar for acetone, acetonitrile and THF; a different trend is detected  
618 for TBA, for which micro-mixing turns out to be less efficient compared with  
619 the other good solvents. It is noteworthy to stress here that the numerical  
620 values in the contour plots must be interpreted as absolute values, since  
621 negative terms may come out from the local value of the abscissas in the  
622 two environments of the quadrature. Indeed, this is proven by looking at  
623 the region in which the turbulence is created and dissipated, which is where  
624 molecular-mixing or micro-mixing occurs. It is clearly less shrunk around  
625 the impinging plane than in other solvents, showing wider spatial gradients  
626 in the mixer domain. This might be induced by the viscosity that in the  
627 case of TBA is shown to be much larger (one order of magnitude) than in  
628 the other solvents. These results, by just looking at the mixing dynamics of  
629 the system, already allows us to predict a different scenario for TBA with  
630 respect to acetone, acetonitrile and THF.

631 Let us move now on the dynamics of aggregation. In the case of the first  
632 three solvents (i.e., acetone, acetonitrile, THF), whose dynamics of mixing,  
633 only depending on their physical properties, is shown to be the same, it is  
634 worthwhile to conduct the following analysis. For the sake of brevity, let us  
635 consider only acetone and a ‘virtual’ solvent, characterized by the acetoni-  
636 trile physical properties (Table 1) and by acetone functional forms of Flory  
637 parameters, namely Eq. (9) and (10). By simulating these two solvents with  
638 the solely Brownian aggregation kernel active, we can quantify the dynamics

639 of self-assembly of polymer molecules into clusters and of small clusters into  
 640 larger clusters (before turbulent aggregation takes over). Although the same  
 641 functional forms of the acetone Flory parameters are considered here also  
 642 for the ‘virtual’ solvent, the results show a very different profile, in terms of  
 643 mean radius of gyration of the NP at the outlet of the mixer. This result  
 644 is depicted in Figure 2 and tells us that, although the dynamics of mix-  
 645 ing is identical between acetone and the ‘virtual’ solvent, the aggregation  
 646 behaves in a very different way. The only physical explanation of that is  
 647 attributable to one physical property and, more specifically, lies on the dif-  
 648 ferent molar volumes of the two solvents (look at Table 1), because the other  
 649 physical properties (density and viscosity) are very similar to each other, as  
 650 also demonstrated by looking at the respective Reynolds number values (see  
 651 Table 1). The molar volumes affect the molar fraction of the mixture,  $x_s$ , as  
 652 reported in Table 3 concerning its mean value, after mixing takes place. The  
 653 Flory parameters functional forms are, in turn, function of molar mixture  
 654 fraction. This analysis demonstrates that the differences between good sol-  
 655 vents about the dynamics of aggregation only depend on Flory parameters.  
 656 Furthermore, it is shown how the modeling approach presented in this work  
 657 can be suitably employed to quantify the relative importance of the different  
 658 mechanisms involved in particles formation.

659 At this point of the current analysis, it is straightforward that the gap  
 660 against experiments must be bridged by suitably adjusting the functional  
 661 forms for  $k_s(x_s)$  and  $\nu_s(x_s)$  for all the solvents investigated here. As outcome  
 662 of the iterative procedure presented in section 3 (see Eqs. (19) and (20) and  
 663 Table 3), the final functional forms of the Flory parameters are determined

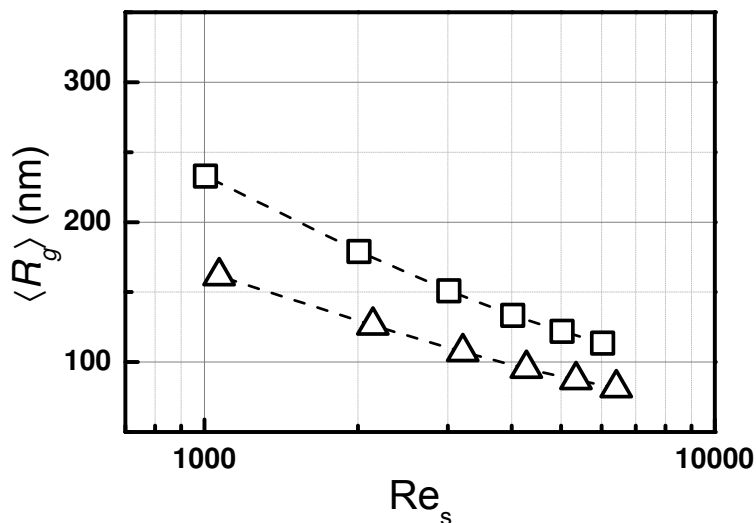


Figure 2: Mean radius of gyration,  $\langle R_g \rangle$ , as a function of Reynolds number referred to the good solvent inlet jet stream, with only Brownian aggregation for PCL initial concentrations equal to 6.0 mg/mL in acetone (triangles) and the ‘virtual’ solvent (squares), characterized by the acetonitrile physical properties and by the acetone functional forms of Flory parameters.

664 and listed in Table 4. These new functional forms are able to guarantee a  
 665 good agreement with experiments, as depicted in Figure 3 (TBA- and THF-  
 666 water systems) and Figure 4 (acetone- and acetonitrile-water systems). The  
 667 range of PCL initial concentrations in the good solvent stream spans from  
 668 3.0 to 9.0 mg mL<sup>-1</sup>. The experimental error bars are also included.

669 Note that the accordance of the current model with experiments is in  
 670 line with the results found out in our previous work (Lavino et al., 2017).  
 671 As far as acetone, acetonitrile and THF are concerned, the agreement is  
 672 excellent starting from medium PCL initial concentration in good solvent  
 673 stream of about 5 mg/mL, namely the predicted NP dimensions are included

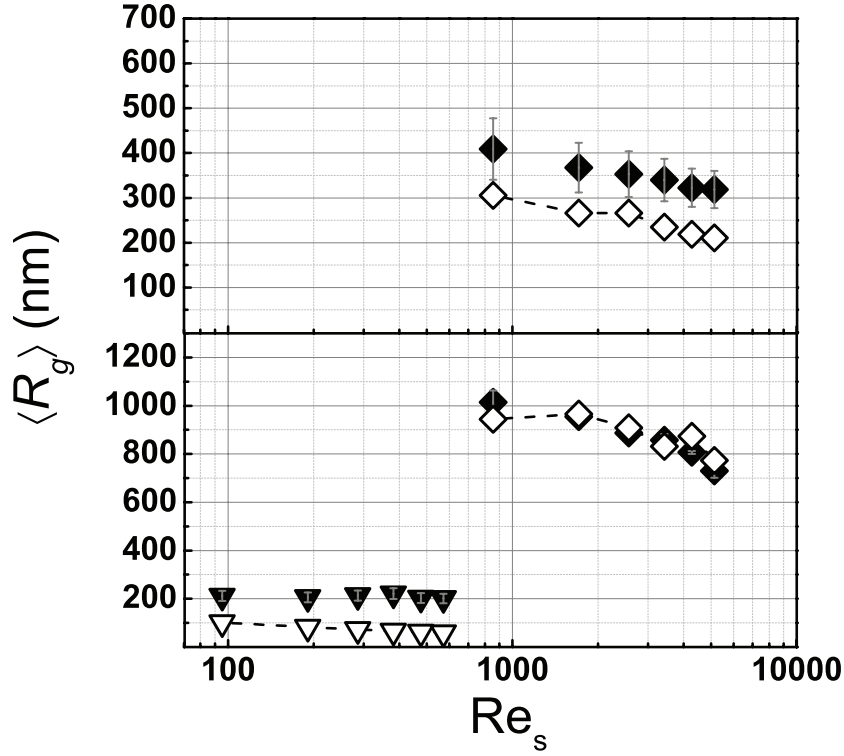


Figure 3: Mean radius of gyration,  $\langle R_g \rangle$ , of the NP exiting the CIJM versus the Reynolds number referred to the good solvent inlet jet stream as measured in experiments (black symbols) and as predicted by the purely-aggregative model (dashed line, empty symbols) for PCL-14000 initial concentrations equal to 3.0 (top panel) and 5.0 (bottom panel) mg/mL in THF (diamonds) and TBA (inverted triangles).

674 into the uncertainty range of the experimental results. In the case of TBA,  
675 where the mixing dynamics is less efficient than in the other three good sol-  
676 vents, the model shows to be transferable, by means of the Flory-Huggins  
677 solubility theory. The experimental profile is qualitatively caught by this  
678 purely-aggregative model, reproducing the negligible effect of the kinetics  
679 on the final mean radius of gyration (flat profile of NP size as function of  
680 the inlet good solvent Reynolds number) (Johnson and Prud'homme, 2003b;

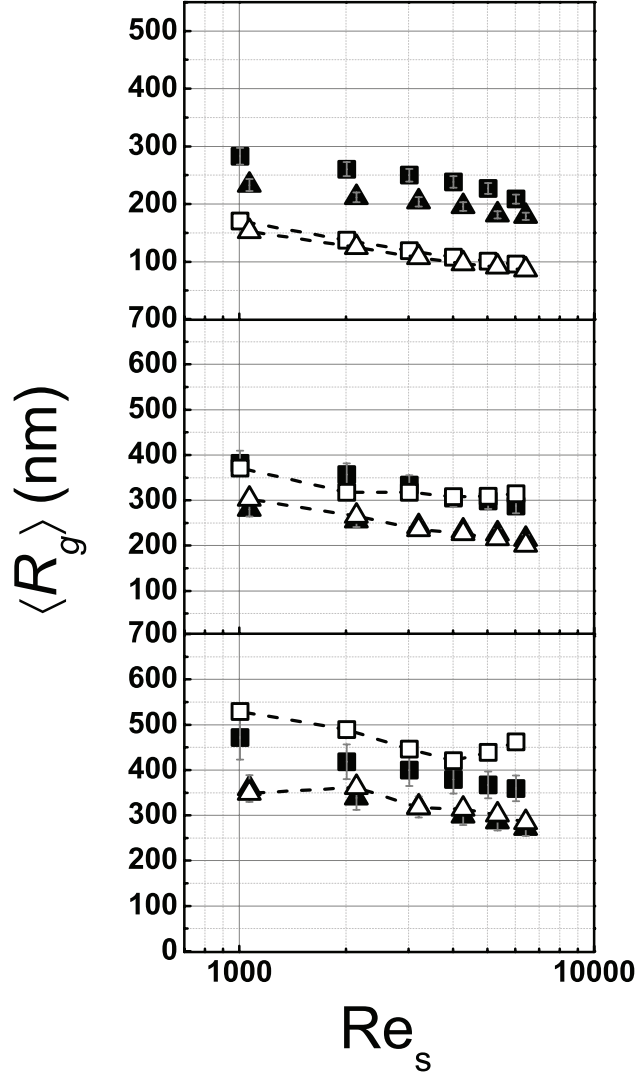


Figure 4: Mean radius of gyration,  $\langle R_g \rangle$ , of the NP exiting the CIJM versus the Reynolds number referred to the good solvent inlet jet stream as measured in experiments (black symbols) and as predicted by the purely-aggregative model (dashed line, empty symbols) for PCL-14000 initial concentrations equal to 3.0 (top), 6.0 (middle) and 9.0 (bottom) mg/mL in acetone (triangles) and acetonitrile (squares) as the good solvents.

681 Zelenková et al., 2015). This behaviour is also explained by looking at the  
 682  $Re_s$  range experienced by TBA in FNP with respect to the other systems,  
 683 as clearly shown in Figures 3 and 4. Indeed,  $Re_s$  ranges of acetone, ace-  
 684 tonitrile, and THF are almost the same as well as one order of magnitude  
 685 higher than TBA inlet Reynolds number, mainly due to the TBA viscosity  
 686 (see Table 1). In the case of TBA,  $Re_s$  value presumes that the turbulence  
 687 is not completely developed inside the CIJM leading to less efficient mixing  
 688 dynamics - as already stated - and, therefore, to a less important effect of  
 689 fluid dynamics on the final mean NP size with respect to the other good sol-  
 690 vent systems, as reproduced by both experiments and simulations. Results  
 691 show, however, a quantitative gap against experiments, which, on the con-  
 692 trary, is not observed in the case of THF (bottom panel in Figure 3) at the  
 693 same PCL initial concentration (5 mg/mL). It is worthwhile to stress that  
 694 this gap cannot be numerically overcome by using the proposed computa-  
 695 tional tuning (described in section 3, in order not to break the physics of the  
 696 system, namely having higher values of Flory parameters for TBA than in  
 697 acetone (look at Figure 5) which, instead, is shown to have a better affinity  
 698 with PCL (lower solubility distance in Hansen phase space). At low initial  
 699 polymer concentration (3 mg/mL in ACT, ACN, and THF and 5 mg/mL  
 700 in TBA), the mismatch observed between experimental data and simulation  
 701 results should be due to nucleation phenomena which at low supersaturation  
 702 ratios dominate over aggregation and that are not explicitly taken into ac-  
 703 count in this purely-aggregative model. At constant PCL inlet concentration  
 704 (around 5 mg/mL), nucleation might be more important for TBA than in the  
 705 other systems, in which turbulence is demonstrated to play a secondary role

706 in the aggregation for PCL inlet concentration under 5 mg/mL by our previ-  
 707 ous CFD analysis (Lavino et al., 2017). The trends reported in Figure 4 are  
 708 consistent with those shown in Figure 3 and with our previous work where  
 709 the current CFD-PBM model was developed and validated. It is instructive  
 710 to point out a deeper analysis regarding the trend observed for the simulated  
 711 data of the acetonitrile case at 9 mg/mL (bottom panel, Figure 4) where our  
 712 simulations show a minimum at high  $Re_s$  values (i.e., high flow rates). This  
 713 trend was also observed in our previous work (Lavino et al., 2017) at very  
 714 high initial PCL concentration in acetone streams and is due to a twofold,  
 715 contrasting effect of turbulence. On one side, indeed, turbulence promotes a  
 716 more efficient mixing leading to smaller nanoparticles; on the other, at high  
 717 initial polymer concentrations, turbulent aggregation dominates, inducing  
 718 the formation of bigger nanoparticles. Contrarily to the acetone case that  
 719 was observed in both experimental and simulated data (please refer to Lavino  
 720 et al. (2017)), for the acetonitrile this starts happening in our simulations  
 721 first, at high flow rates, which means that the turbulent aggregation is over-  
 722 estimated by the current model. This leads us to conclude that a step-wise  
 723 aggregation efficiency of the PBM source term fails in the description of the  
 724 particle formation process when the system is either too diluted (nucleation  
 725 phenomena dominate) or too concentrated at high flow rates (i.e., high  $Re_s$   
 726 number) and works very well otherwise.

727 The Flory exponent profiles (Table 4) are depicted in Figure 5. The  
 728 inset shows the  $\nu_s$  values corresponding to the different mean good solvent  
 729 molar fractions  $\bar{x}_s$  (discrete symbols), assuming the perfect mixing between  
 730 the good and the bad solvent streams, already mentioned in the section 3.

731 This perfect mixing condition corresponds to a single good solvent volume  
 732 fraction value of 0.5 but different molar fractions, due to the different molar  
 733 volumes of the good solvents. It is important to point out here that, from  
 734 a qualitative point of view, the effect of the good solvent on the final mean  
 735 NP size can be predicted looking at the Flory exponent evaluated at the  
 736 mean good solvent molar fraction  $\nu_s(\bar{x}_s)$ . At the mean good solvent molar  
 737 fraction  $\bar{x}_s$ , the inset shows the following relation for different good solvents:  
 738  $\nu_{\text{THF}}(\bar{x}_{\text{THF}}) > \nu_{\text{ACN}}(\bar{x}_{\text{ACN}}) > \nu_{\text{ACT}}(\bar{x}_{\text{ACT}}) > \nu_{\text{TBA}}(\bar{x}_{\text{TBA}})$ . This justifies,  
 739 indeed, the fact that PCL aggregates more in THF than in acetonitrile, in  
 740 acetone and finally in TBA at constant PCL initial concentration, in line  
 741 with experiments (Ferri et al., 2017; Zelenková et al., 2015). Therefore,  
 742 the approach described here is able to reproduce the experimental evidences  
 743 highlighting the fundamental role played by the good solvent molar fraction.  
 744 Note that the  $\nu_s(\bar{x}_s)$  values are very close to each other, denoting the high  
 745 sensitivity of the Flory exponent on final mean NP size.

746 Figure 5 also depicts the affinity order found out in terms of HSP and  
 747 solubility distance from PCL shown in Table 2, namely  $\text{THF} > \text{ACT} >$   
 748  $\text{TBA} > \text{ACN}$  for which the solubility distances from PCL are respectively  
 749 1.0, 6.5, 7.4 and 13.8 MPa<sup>1/2</sup>. Hence, at constant molar fraction,  $\nu_s$  is di-  
 750 rectly proportional to the good solvent affinity with PCL (in terms of sol-  
 751 ubility distance). This implies that the polymer chain increases in size and  
 752 assumes a more stretched conformation, according to the thermodynamics  
 753 of real polymers in solution. However, operating at constant good-solvent-  
 754 to-water ratio in volume leads to a mean good solvent molar fraction in the  
 755 order:  $\bar{x}_{\text{ACN}} > \bar{x}_{\text{ACT}} > \bar{x}_{\text{THF}} > \bar{x}_{\text{TBA}}$ , because of the different molar volumes

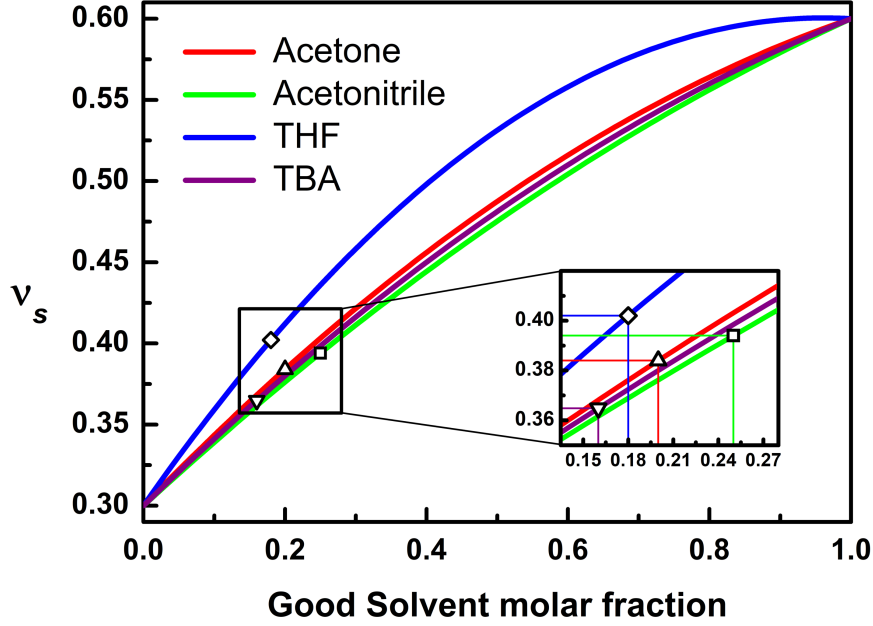


Figure 5: Flory exponent  $\nu_s$  profiles in function of good solvent molar fraction for acetone (red), acetonitrile (green), THF (blue) and TBA (purple) (Table 4). The discrete symbols correspond to the Flory exponent at the outlet mean good solvent molar fraction  $\nu_s(\bar{x}_s)$  (inset).

756 of the good solvents. This affects the Flory parameters and, consequently,  
 757 aggregation, the final NP size and CMD.

758 In Figure 6 the mean-squared radius of gyration of a NP is reported  
 759 for acetone (red), acetonitrile (green), THF (blue) and TBA (purple) in  
 760 function of the aggregation number. The crossover between the red and  
 761 green profiles (acetone and acetonitrile) shows the two different tendencies  
 762 and contributions in case of single PCL molecule ( $\llbracket R_g(n = 1) \rrbracket$  higher in  
 763 acetone) and at high aggregation number,  $n$ , in which  $\llbracket R_g(n) \rrbracket$  is higher

764 in acetonitrile than in acetone. This means that, despite the single PCL  
 765 macromolecule occupies a smaller volume in acetonitrile, the PCL NP is  
 766 bigger in acetonitrile, namely more PCL macromolecules form the same  
 767 cluster (or NP) in acetonitrile ( $m^{(1)}/m^{(0)}$  is therefore greater than in ace-  
 768 tone). Therefore, the Flory theory combined together with the solubility  
 769 affinity with PCL implies the following order of the single PCL macro-  
 770 molecule dimension: THF > ACT > ACN > TBA, as also indicated by  
 771 the  $S_f$  values in Table 3. However, the combination of good solvent mo-  
 772 lar volume (leading to different molar fractions) and the aggregation kernels  
 773 (dependent on Flory parameters) produces the following aggregation order:  
 774 THF > ACN > ACT > TBA.

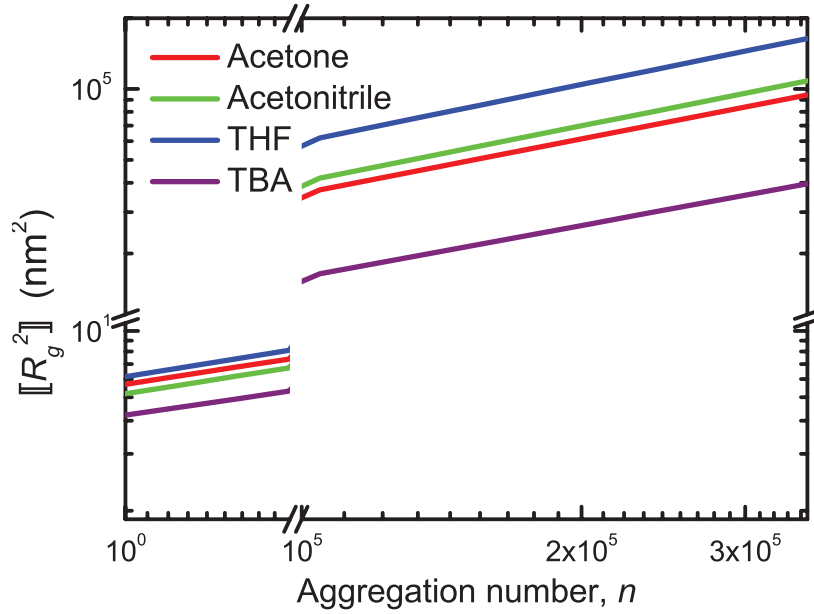


Figure 6: Mean squared radius of gyration,  $[R_g^2]$ , as a function of the number of molecules (Eq. (8)) that form a cluster (aggregation number,  $n$ ) for acetone (red), acetonitrile (green), THF (blue) and TBA (purple) at the respective outlet mean good solvent molar fraction  $\bar{x}_s$ .

## 775 5. Conclusions

776 In this work the effect of different good solvents in flash nano-precipitation  
777 (FNP) is studied, from a modeling point of view. A population balance model  
778 (PBM) based on molecules as building blocks is coupled with computational  
779 fluid dynamics (CFD) and implemented in a commercial CFD code. Mo-  
780 ments of the cluster mass distribution (CMD) are transported and closed  
781 by using the quadrature method of moments (QMOM) (Marchisio and Fox,  
782 2013). The CMD is defined in such a way that it represents the number of  
783 polymer molecules inside a cluster/NP. The turbulent mixing effects on NP  
784 formation are accounted for with the direct quadrature method of moments  
785 coupled with the interaction and exchange with the mean (DQMOM-IEM)  
786 method, in line with our reference work, in which this modeling approach  
787 was tested and validated (Lavino et al., 2017).

788 The novelty of the current approach consists in coupling PBM and CFD  
789 with thermodynamics of polymers in solution. More specifically, the Flory-  
790 Huggins interaction parameter  $\chi$  is considered, taking into account therefore  
791 the energetic contribution related to the polymer in the mixture, and is here  
792 correlated to the prediction of the mean radius of gyration of the NP. All this  
793 is done by taking advantage of the solubility theory in mixtures, in terms of  
794 Hansen solubility parameters (HSP). In this way, different good solvents are  
795 studied, with water as anti-solvent and poly- $\epsilon$ -caprolactone (PCL) as solute,  
796 in confined impinging jets mixer (CIJM). Four different good solvents are  
797 considered: acetone (ACT), acetonitrile (ACN), tetrahydrofuran (THF) and  
798 tert-butanol (TBA), taking the acetone as the reference solvent, being this  
799 one already investigated at the molecular scale with molecular dynamics in

800 a previous work (Di Pasquale et al., 2014).

801 Thanks to the proposed approach, kinetics and thermodynamics are in-  
802 tertwined in a unique modeling tool used to investigate separately the dy-  
803 namics of mixing from the dynamics of aggregation, addressing the main  
804 factors that play a key role in such a complex process. CFD simulations  
805 demonstrate that acetone, acetonitrile and THF are characterized by the  
806 same macro- and micro-mixing dynamics, whereas TBA shows a different  
807 micro-mixing behaviour, strongly dependent on its viscosity, that is one or-  
808 der of magnitude higher than the other solvents and water. Results also show  
809 that the molar volume, combined together with the HSP, provides a good  
810 prediction of the final mean NP size when different good solvents are em-  
811 ployed in FNP. Furthermore, functional forms for the Flory parameters are  
812 determined, by combining the Flory-Huggins solubility theory with a suitable  
813 computational tuning. In this way, it is shown that the proposed modeling  
814 approach is transferable and adaptable to different scenarios, leading to a  
815 good prediction of the experimental results from quantitative and qualita-  
816 tive points of view. This is valid also in the case of TBA which presents a  
817 different mixing dynamics that, in turn, affects the final NP profile in func-  
818 tion of the inlet Reynolds number. The detected limitations, in terms of  
819 accordance with experiments, might be overcome by introducing nucleative  
820 effects in the aggregation source term of the PBM. In conclusion, although  
821 the phenomena involved are very complex and this is not indeed the ultimate  
822 model for FNP, this model is able to capture the main effects experimentally  
823 observed since both kinetics and thermodynamics are considered.

824 Future work may be done by investigating these good solvent-water sys-

825 tems at the molecular scale with full-atom and coarse-grained molecular dy-  
826 namics simulations, aiming at confirming or refining the results obtained in  
827 this work, with more detailed molecular models.

## 828 Appendix

### 829 Appendix A. Mixing modeling and micro-mixing variance

830 In this appendix, further mathematical details concerning the mixing  
831 modeling are provided. More specifically, it will be shown how the micro-  
832 mixing variance can be related to the mixing transport equation, in particular  
833 to one of its terms: the micro-mixing term. In this modeling framework, as  
834 reported in the main text, the mixture fraction is transported by means of  
835 the direct quadrature method of moment coupled with the interaction and  
836 exchange with the mean method (DQMOM-IEM) (Marchisio and Fox, 2013).

837 Besides the micro-mixing model introduced in the main text in section  
838 2.1, a large-scale or macro-scale variance  $\langle \xi'^2 \rangle_{macro}$  is defined as follows:

$$\langle \xi'^2 \rangle_{macro} = (\langle \xi \rangle - \bar{\xi})^2, \quad (A.1)$$

839 quantifying how different the local mean mixture fraction  $\langle \xi \rangle$  is from the ideal  
840 value  $\bar{\xi}$  that it would assume if the mixing were perfect. In the analyzed case,  
841 for instance,  $\bar{\xi}_v = 0.5$  in volume. For the analyzed cases, this tells us that  
842 the macro-mixing is very efficient, leading the macro-mixing variance to zero  
843 in almost all the CIJM, as shown in Figure 1.

844 The micro-mixing variance is defined as (Liu and Fox, 2006):

$$\langle \xi'^2 \rangle = \langle \xi^2 \rangle - \langle \xi \rangle^2. \quad (A.2)$$

845 We can rearrange the last expression as follows:

$$\begin{aligned}
\langle \xi'^2 \rangle &= \langle \xi^2 \rangle - \langle \xi \rangle^2 = p_1 \xi_1^2 + p_2 \xi_2^2 - (p_1 \xi_1 + p_2 \xi_2)^2 = \\
&= p_1 \xi_1^2 (1 - p_1) + p_2 \xi_2^2 (1 - p_2) - 2p_1 p_2 \xi_1 \xi_2 = \\
&= p_1 p_2 (\xi_1^2 + \xi_2^2 - 2\xi_1 \xi_2) = p_1 p_2 (\xi_2 - \xi_1)^2, \quad (\text{A.3})
\end{aligned}$$

846 where the property  $p_1 = 1 - p_2$  is applied. By using the results shown in  
847 Eq. (A.3), the first term on right hand side of Eq. (5) that contains the micro-  
848 mixing rate can be expressed as follows (the fluid density  $\bar{\rho}$  is here omitted  
849 for simplicity of notation):

$$\gamma_M p_1 p_2 (\xi_2 - \xi_1) = \frac{\gamma_M}{(\xi_2 - \xi_1)} \langle \xi'^2 \rangle, \quad (\text{A.4})$$

850 strictly dependent on the micro-mixing variance  $\langle \xi'^2 \rangle$ . The quantity ex-  
851 pressed in Eq. (A.4) is the one reported in the contour plots in Figure 1  
852 and can be thought of as a measure of how the micro-mixing variance is dis-  
853 sipated by turbulence (included in the definition of  $\gamma_M$ ) at the micro-scale.

## 854 **Acknowledgements**

855 This contribution was identified by R. Bertrum Diemer Jr (University  
856 of Delaware) as the Best Presentation in the session “Population Balance  
857 Modeling for Particle Formation Processes: Nucleation, Aggregation and  
858 Breakage Kernels” of the 2018 AIChE Annual Meeting in Pittsburgh. Com-  
859 putational resources were provided by HPC@POLITO, a project of Academic  
860 Computing within the Department of Control and Computer Engineering at  
861 the Politecnico di Torino (<http://www.hpc.polito.it>).

## 862 **References**

- 863 Andersson, B., Andersson, R., Hakansson, L., Mortensen, M., Sudiyo, R.,  
864 van Wachem, B., 2012. Computational Fluid Dynamics for Engineering.  
865 Cambridge: Cambridge University Press.
- 866 Baldyga, J., Orciuch, W., 2001. Some hydrodynamic aspects of precipi-  
867 tation. Powder Technology 121, 9–19. doi:[https://doi.org/10.1016/](https://doi.org/10.1016/S0032-5910(01)00368-0)  
868 [S0032-5910\(01\)00368-0](https://doi.org/10.1016/S0032-5910(01)00368-0).
- 869 Barresi, A.A., Vanni, M., Fissore, D., Zelenková, T., 2015. Thakur VK,  
870 Thaku MK. Handbook of Polymers for Pharmaceutical Technologies.  
871 Hoboken: John Wiley & Sons, Ltd. chapter Synthesis and preservation  
872 of polymer nanoparticles for pharmaceutical applications. pp. 229–280.  
873 doi:<https://doi.org/10.1002/9781119041412.ch9>.
- 874 Bhattacharjee, S., 2016. Dls and zeta potential – what they are and what  
875 they are not? Journal of Controlled Release 235, 337 – 351. doi:<https://doi.org/10.1016/j.jconrel.2016.06.017>.

- 877 Bordes, C., Fréville, V., Ruffin, E., Marote, P., Gauvrit, J.Y., Briançon,  
878 S., Lantéri, P., 2010. Determination of poly( $\epsilon$ -caprolactone) solubil-  
879 ity parameters: Application to solvent substitution in a microencapsu-  
880 lation process. *International Journal of Pharmaceutics* 383, 236–243.  
881 doi:<https://doi.org/10.1016/j.ijpharm.2009.09.023>.
- 882 Celasco, E., Valente, I., Marchisio, D.L., Barresi, A.A., 2014. Dynamic light  
883 scattering and x-ray photoelectron spectroscopy characterization of pe-  
884 gylated polymer nanocarriers: Internal structure and surface properties.  
885 *Langmuir* 30, 8326–8335. doi:<https://doi.org/10.1021/la501198v>.
- 886 Cheng, J.C., Vigil, R.D., Fox, R.O., 2010. A competitive aggregation model  
887 for flash nanoprecipitation. *Journal of Colloid and Interface Science* 351,  
888 330–342. doi:<https://doi.org/10.1016/j.jcis.2010.07.066>.
- 889 Choi, Y.J., Chung, S.T., Oh, M., Kim, H.S., 2005. Investigation of cristalliza-  
890 tion in a jet y-mixer by a hybrid computational fluid dynamics and process  
891 simulation approach. *Cristal Growth & Design* 5, 959–968. doi:<https://doi.org/10.1021/cg049670x>.
- 893 Das, M., Saxena, N., Dwivedi, P.D., 2009. Emerging trends of nanoparticles  
894 application in food technology: Safety paradigms. *Nanotoxicology* 3, 10–  
895 18. doi:<https://doi.org/10.1080/17435390802504237>.
- 896 Demetzos, C., 2016. *Pharmaceutical Nanotechnology*. Singapore: Adis.
- 897 Di Pasquale, N., Marchisio, D.L., Barresi, A.A., 2012. Model validation for  
898 precipitation in solvent-displacement processes. *Chemical Engineering Sci-*  
899 *ence* 84, 671–683. doi:<https://doi.org/10.1016/j.ces.2012.08.043>.

- 900 Di Pasquale, N., Marchisio, D.L., Barresi, A.A., Carbone, P., 2014. Sol-  
901 vent structuring and its effect on the polymer structure and processabil-  
902 ity: the case of water-acetone poly- $\epsilon$ -caprolactone mixtures. *Journal of*  
903 *Physical Chemistry B* 118, 13258–13267. doi:[https://doi.org/10.1021/](https://doi.org/10.1021/jp505348t)  
904 [jp505348t](https://doi.org/10.1021/jp505348t).
- 905 Elimelech, M., Gregory, J., Jia, X., Williams, R., 1998. *Particle Deposi-*  
906 *tion and Aggregation: Measurement, Modelling and Simulation*. Woburn:  
907 Butterworth-Heinemann.
- 908 Favre, A., 1965. Equations des gaz turbulents compressibles i. formes  
909 générales. *Journal de Mecanique* 4, 361–390.
- 910 Ferri, A., Kumari, N., Peila, R., Barresi, A.A., 2017. Production of menthol-  
911 loaded nanoparticles by solvent displacement. *The Canadian Journal of*  
912 *Chemical Engineering* 95, 1690–1706. doi:[https://doi.org/10.1002/](https://doi.org/10.1002/cjce.22867)  
913 [cjce.22867](https://doi.org/10.1002/cjce.22867).
- 914 Flory, P., 1953. *Principles of Polymer Chemistry*. Ithaca: Cornell University  
915 Press.
- 916 Fox, R.O., 2003. *Computational Models for Turbulent Reacting Flows*. Cam-  
917 bridge: Cambridge University Press. doi:[10.1017/CB09780511610103](https://doi.org/10.1017/CB09780511610103).
- 918 Gartner, T.E., Jayaraman, A., 2018. Macromolecular ‘size’ and ‘hard-  
919 ness’ drives structure in solvent-swollen blends of linear, cyclic, and star  
920 polymers. *Soft Matter* 14, 411–423. doi:[https://doi.org/10.1039/](https://doi.org/10.1039/C7SM02199B)  
921 [C7SM02199B](https://doi.org/10.1039/C7SM02199B).

- 922 Gavi, E., Marchisio, D.L., Barresi, A.A., 2007. Cfd modelling and scale-  
923 up of confined impinging jet reactors. *Chemical Engineering Science* 62,  
924 2228–2241. doi:<https://doi.org/10.1016/j.ces.2006.12.077>.
- 925 Gradl, J., Schwarzer, H.C., Schwertfirm, F., Manhart, M., Peukert, W., 2006.  
926 Precipitation of nanoparticles in a t-mixer: coupling the particle popula-  
927 tion dynamics with hydrodynamics through direct numerical simulation.  
928 *Chemical Engineering and Processing: Process Intensification* 45, 908–916.  
929 doi:<https://doi.org/10.1016/j.cep.2005.11.012>.
- 930 Hans, M.L., Lowman, A.M., 2002. Biodegradable nanoparticles for drug de-  
931 livery and targeting. *Current Opinion in Solid State and Materials Science*  
932 6, 319–327. doi:[https://doi.org/10.1016/S1359-0286\(02\)00117-1](https://doi.org/10.1016/S1359-0286(02)00117-1).
- 933 Hansen, C.M., 2007. Hansen Solubility Parameters: A User’s Handbook (2nd  
934 edition). Boca Raton: CRC Press.
- 935 Hildebrand, J., Scott, R.L., 1950. Solubility of Nonelectrolytes (3rd edition).  
936 New York: Reinhold.
- 937 Johnson, B.K., Prud’homme, R.K., 2003a. Chemical processing and micro-  
938 mixing in confined impinging jets. *AIChE Journal* 49, 2264–2282.  
939 doi:<https://doi.org/10.1002/aic.690490905>.
- 940 Johnson, B.K., Prud’homme, R.K., 2003b. Flash nano-precipitation of or-  
941 ganic actives and block copolymers using a confined impinging jets mixer.  
942 *Australian Journal of Chemistry* 56, 1021–1024. doi:<https://doi.org/10.1071/CH03115>.  
943

- 944 Lavino, A.D., Banetta, L., Carbone, P., Marchisio, D.L., 2018. Ex-  
945 tended charge-on-particle optimized potentials for liquid simulation ace-  
946 tone model: The case of acetone–water mixtures. *The Journal of Physical*  
947 *Chemistry B* 122, 5234–5241. doi:[https://doi.org/10.1021/acs.jpcc.](https://doi.org/10.1021/acs.jpcc.8b01293)  
948 8b01293.
- 949 Lavino, A.D., Carbone, P., Marchisio, D.L., 2020. Martini coarse-grained  
950 model for poly- $\epsilon$ -caprolactone in acetone-water mixtures. *The Canadian*  
951 *Journal of Chemical Engineering* 98, 1868–1879. doi:[https://doi.org/](https://doi.org/10.1002/cjce.23761)  
952 10.1002/cjce.23761.
- 953 Lavino, A.D., Di Pasquale, N., Carbone, P., Barresi, A.A., Marchisio, D.L.,  
954 2015. Simulation of macromolecule self-assembly in solution: A multiscale  
955 approach. *AIP Conference Proceedings* 1695, 020036. doi:[https://doi.](https://doi.org/10.1063/1.4937314)  
956 [org/10.1063/1.4937314](https://doi.org/10.1063/1.4937314).
- 957 Lavino, A.D., Di Pasquale, N., Carbone, P., Marchisio, D.L., 2017. A novel  
958 multiscale model for the simulation of polymer flash nano-precipitation.  
959 *Chemical Engineering Science* 171, 485–494. doi:[https://doi.org/10.](https://doi.org/10.1016/j.ces.2017.04.047)  
960 1016/j.ces.2017.04.047.
- 961 Lavino, A.D., Marchisio, D.L., Vanni, M., Ferri, A., Barresi, A.A., 2019.  
962 Nanoparticles production in continuous flow devices - modelling and ex-  
963 perimental insights into continuous flow-based processes. *Chimica Oggi -*  
964 *Chemistry Today* 37, 8–11.
- 965 Le Roy Boehm, A.L., Zerrouk, R., Fessi, H., 2000. Poly epsilon-caprolactone  
966 nanoparticles containing a poorly soluble pesticide: formulation and sta-

967 bility study. *Journal of Microencapsulation* 17, 195–205. doi:[https:](https://doi.org/10.1080/026520400288436)  
968 [//doi.org/10.1080/026520400288436](https://doi.org/10.1080/026520400288436).

969 Lince, F., Marchisio, D.L., Barresi, A.A., 2008. Strategies to control the par-  
970 ticle size distribution of poly- $\epsilon$ -caprolactone nanoparticles for pharmaceu-  
971 tical applications. *Journal of Colloid and Interface Science* 322, 505–515.  
972 doi:<https://doi.org/10.1016/j.jcis.2008.03.033>.

973 Lince, F., Marchisio, D.L., Barresi, A.A., 2009. Smart mixers and reac-  
974 tors for the production of pharmaceutical nanoparticles: Proof of con-  
975 cept. *Chemical Engineering Research and Design* 87, 543–549. doi:[https:](https://doi.org/10.1016/j.cherd.2008.11.009)  
976 [//doi.org/10.1016/j.cherd.2008.11.009](https://doi.org/10.1016/j.cherd.2008.11.009).

977 Lince, F., Marchisio, D.L., Barresi, A.A., 2011. A comparative study for  
978 nanoparticle production with passive mixers via solvent-displacement: Use  
979 of cfd models for optimization and design. *Chemical Engineering and*  
980 *Processing: Process Intensification* 50, 356–368. doi:[https://doi.org/](https://doi.org/10.1016/j.cep.2011.02.015)  
981 [10.1016/j.cep.2011.02.015](https://doi.org/10.1016/j.cep.2011.02.015).

982 Liu, Y., Cheng, C., Prud'homme, R.K., Fox, R.O., 2008. Mixing in a multi-  
983 inlet vortex mixer (mivm) for flash nano-precipitation. *Chemical Engineer-*  
984 *ing Science* 63, 2829–2842. doi:[https://doi.org/10.1016/j.ces.2007.](https://doi.org/10.1016/j.ces.2007.10.020)  
985 [10.020](https://doi.org/10.1016/j.ces.2007.10.020).

986 Liu, Y., Fox, R.O., 2006. Cfd predictions for chemical processing in a confined  
987 impinging-jets reactor. *AIChE Journal* 52, 731–744. doi:[https://doi.](https://doi.org/10.1002/aic.10633)  
988 [org/10.1002/aic.10633](https://doi.org/10.1002/aic.10633).

- 989 Marchisio, D.L., Fox, R.O., 2005. Solution of population balance equations  
990 using the direct quadrature method of moments. *Journal of Aerosol Science*  
991 36, 43–73. doi:<https://doi.org/10.1016/j.jaerosci.2004.07.009>.
- 992 Marchisio, D.L., Fox, R.O., 2013. *Computational Models for Polydisperse*  
993 *Particulate and Multiphase Flows*. Cambridge: Cambridge University  
994 Press.
- 995 Marchisio, D.L., Omegna, F., Barresi, A.A., 2009. Production of tio2  
996 nanoparticles with controlled characteristics by means of a vortex reac-  
997 tor. *Chemical Engineering Journal* 146, 456–465. doi:[https://doi.org/](https://doi.org/10.1016/j.cej.2008.10.031)  
998 [10.1016/j.cej.2008.10.031](https://doi.org/10.1016/j.cej.2008.10.031).
- 999 Marchisio, D.L., Omegna, F., Barresi, A.A., Bowen, P., 2008. Effect of  
1000 mixing and other operating parameters in sol-gel processes. *Industrial &*  
1001 *Engineering Chemistry Research* 47, 7202–7210. doi:[https://doi.org/](https://doi.org/10.1021/ie800217b)  
1002 [10.1021/ie800217b](https://doi.org/10.1021/ie800217b).
- 1003 Martin, T.B., Jayaraman, A., 2016. Using theory and simulations to calcu-  
1004 late effective interactions in polymer nanocomposites with polymer-grafted  
1005 nanoparticles. *Macromolecules* 49, 9684–9692. doi:[https://doi.org/10.](https://doi.org/10.1021/acs.macromol.6b01920)  
1006 [1021/acs.macromol.6b01920](https://doi.org/10.1021/acs.macromol.6b01920).
- 1007 Massella, D., Celasco, E., Salaün, F., Ferri, A., Barresi, A.A., 2018. Overcom-  
1008 ing the limits of flash nanoprecipitation: effective loading of hydrophilic  
1009 drug into polymeric nanoparticles with controlled structure. *Polymers* 10,  
1010 1092. doi:<https://doi.org/10.3390/polym10101092>.

1011 Nelson, G., 2002. Application of microencapsulation in textiles. *International*  
 1012 *Journal of Pharmaceutics* 242, 55–62. doi:[https://doi.org/10.1016/](https://doi.org/10.1016/S0378-5173(02)00141-2)  
 1013 [S0378-5173\(02\)00141-2](https://doi.org/10.1016/S0378-5173(02)00141-2).

1014 Petitti, M., Vanni, M., Barresi, A.A., 2008. Controlled release of drug en-  
 1015 capsulated as a solid core: Theoretical model and sensitivity analysis.  
 1016 *Chemical Engineering Research and Design* 86, 1294–1300. doi:[https:](https://doi.org/10.1016/j.cherd.2008.05.008)  
 1017 [//doi.org/10.1016/j.cherd.2008.05.008](https://doi.org/10.1016/j.cherd.2008.05.008).

1018 Prasad, R., Kumar, V., Prasad, K.S., 2014. Nanotechnology in sustain-  
 1019 able agriculture: Present concerns and future aspects. *African Journal*  
 1020 *of Biotechnology* 13, 705–713. doi:[https://doi.org/10.5897/AJBX2013.](https://doi.org/10.5897/AJBX2013.13554)  
 1021 [13554](https://doi.org/10.5897/AJBX2013.13554).

1022 Rubinstein, M., Colby, R.H., 2003. *Polymer Physics*. Oxford: Oxford Uni-  
 1023 versity Press.

1024 Saad, W.S., 2007. Drug nanoparticle formation via flash nanoprecipitation:  
 1025 Conjugation to encapsulate and control the release of paclitaxel. Ph.D.  
 1026 thesis. Princeton University.

1027 Saad, W.S., Prud’homme, R.K., 2016. Principles of nanoparticle formation  
 1028 by flash nanoprecipitation. *Nano Today* 11, 212–227. doi:[https://doi.](https://doi.org/10.1016/j.nantod.2016.04.006)  
 1029 [org/10.1016/j.nantod.2016.04.006](https://doi.org/10.1016/j.nantod.2016.04.006).

1030 Valente, I., Celasco, E., Marchisio, D.L., Barresi, A.A., 2012a. Nanopre-  
 1031 cipitation in confined impinging jets mixers: Production, characteriza-  
 1032 tion and scale-up of pegylated nanospheres and nanocapsules for phar-

1033      maceutical use. Chemical Engineering Science 77, 217–227. doi:[https:](https://doi.org/10.1016/j.ces.2012.02.050)  
1034      [//doi.org/10.1016/j.ces.2012.02.050](https://doi.org/10.1016/j.ces.2012.02.050).

1035      Valente, I., Stella, B., Marchisio, D.L., Dosio, F., Barresi, A.A., 2012b. Pro-  
1036      duction of pegylated nanocapsules through solvent-displacement in con-  
1037      fined impinging jets mixers. Journal of Pharmaceutical Sciences 101, 2490–  
1038      2501. doi:<https://doi.org/10.1002/jps.23167>.

1039      Who, C., Jim, T., Gan, Z., Zhao, Y., Wang, S., 2000. A heterogeneous  
1040      catalytic kinetics for enzymatic biodegradation of poly( $\epsilon$ -caprolactone)  
1041      nanoparticles in aqueous solution. Polymer 41, 3593–3597. doi:[https:](https://doi.org/10.1016/S0032-3861(99)00586-8)  
1042      [//doi.org/10.1016/S0032-3861\(99\)00586-8](https://doi.org/10.1016/S0032-3861(99)00586-8).

1043      Wu, X., Guy, R.H., 2009. Applications of nanoparticles in topical drug  
1044      delivery and in cosmetics. Journal of Drug Delivery Science and Technology  
1045      19, 371–384. doi:[https://doi.org/10.1016/S1773-2247\(09\)50080-9](https://doi.org/10.1016/S1773-2247(09)50080-9).

1046      Zelenková, T., Barresi, A.A., Fissore, D., 2015. On the use of *tert*-  
1047      butanol/water cosolvent systems in production and freeze-drying of poly- $\epsilon$ -  
1048      caprolactone nanoparticles. Journal of Pharmaceutical Sciences 104, 178–  
1049      190. doi:<https://doi.org/10.1002/jps.24271>.

1050      Zelenková, T., Fissore, D., Marchisio, D.L., Barresi, A.A., 2014. Size  
1051      control in production and freeze-drying of poly- $\epsilon$ -caprolactone nanopar-  
1052      ticles. Journal of Pharmaceutical Sciences 103, 1839–1850. doi:[https:](https://doi.org/10.1002/jps.23960)  
1053      [//doi.org/10.1002/jps.23960](https://doi.org/10.1002/jps.23960).

1054      Zelenková, T., Mora, M.J., Barresi, A.A., Granero, G.E., Fissore, D., 2018.  
1055      On the production of chitosan-coated polycaprolactone nanoparticles in a

1056 confined impinging jet reactor. *Journal of Pharmaceutical Sciences* 107,  
1057 1157–1166. doi:<https://doi.org/10.1016/j.xphs.2017.11.020>.